The Journal of Neuroscience

https://jneurosci.msubmit.net

JN-RM-1606-20R2

Brief sensory deprivation triggers cell type-specific structural and functional plasticity in olfactory bulb neurons

Elisa Galliano, University Of Cambridge
Christiane Hahn, King's College London
Lorcan Browne, King's College London
Paula Rodriguez Villamayor, King's College London
Candida Tufo, King's College London
Andres Crespo, King's College London
Matthew Grubb, King's College London

Commercial Interest:

Brief sensory deprivation triggers cell type-specific structural and functional plasticity in olfactory bulb neurons

Abbreviated title: Rapid olfactory deprivation-induced plasticity

Elisa Galliano[1,2], Christiane Hahn[1], Lorcan P. Browne[1], Paula R. Villamayor[1], Candida Tufo[1], Andres Crespo[1] and Matthew S. Grubb[1]

1. Centre for Developmental Neurobiology, Institute of Psychiatry, Psychology & Neuroscience, King's College London, New Hunt's House, Guy's Campus, London SE1 1UL, UK

2. Department of Physiology, Development and Neuroscience, University of Cambridge, Downing Street, Cambridge CB2 3DY , UK

Correspondence should be addressed to Elisa Galliano (eg542@cam.ac.uk) and Matthew Grubb (matthew.grubb@kcl.ac.uk)

Author Contributions: Designed research: EG, MSG
Performed research: EG, CH, LB, PRV, CT, AC
Analysed data: EG, CH, LB, PRV, CT, MSG
Wrote the paper: EG, MSG

Figures: 8
Tables: 5
Abstract: 214 words
Introduction: 647 words
Discussion: 1383 words

Financial interests or conflicts of interest: none

ACKNOWLEDGEMENTS

This work was supported by a Sir Henry Wellcome Fellowship (103044) to EG, a Wellcome Trust Career Development Fellowship (088301), BBSRC grant (BB/N014650/1) and ERC Consolidator Grant (725729; FUNCOPLAN) to MSG, and a Medical Research Council 4-year PhD studentship to CH. We wish to thank Mark Evans and Rosie Sammons for help with 3D tracing in Fiji, Annisa Chand for instructions on nose plug manufacture, and Maxim Volgushev for Matlab code. Venki Murthy and all members of the Grubb, Murthy and Galliano laboratories provided helpful discussions, while Juan Burrone and Sue Jones made invaluable comments on the manuscript.

41 **ABSTRACT**

Can alterations in experience trigger different plastic modifications in neuronal structure and function, and if so, how do they integrate at the cellular level? To address this question, we interrogated circuitry in the mouse olfactory bulb responsible for the earliest steps in odour processing. We induced experience-dependent plasticity in mice of either sex by blocking one nostril for a day, a minimally-invasive manipulation which leaves the sensory organ undamaged and is akin to the natural transient blockage suffered during common mild rhinal infections. We found that such brief sensory deprivation produced structural and functional plasticity in one highly specialised bulbar cell type: axon-bearing dopaminergic neurons in the glomerular layer. After 24 h naris occlusion, the axon initial segment (AIS) in bulbar dopaminergic neurons became significantly shorter, a structural modification that was also associated with a decrease in intrinsic excitability. These effects were specific to the AIS-positive dopaminergic subpopulation, because no experience-dependent alterations in intrinsic excitability were observed in AIS-negative dopaminergic cells. Moreover, 24 h naris occlusion produced no structural changes at the AIS of bulbar excitatory neurons – mitral/tufted and external tufted cells – nor did it alter their intrinsic excitability. By targeting excitability in one specialised dopaminergic subpopulation, experience-dependent plasticity in early olfactory networks might act to fine-tune sensory processing in the face of continually fluctuating inputs.

42

SIGNIFICANCE STATEMENT

Sensory networks need to be plastic so they can adapt to changes in incoming stimuli. To see how cells in mouse olfactory circuits can change in response to sensory challenges, we blocked a nostril for just one day – a naturally-relevant manipulation akin to the deprivation that occurs with a mild cold. We found that this brief deprivation induces forms of axonal and intrinsic functional plasticity in one specific olfactory bulb cell subtype: axon-bearing dopaminergic interneurons. In contrast, intrinsic properties of axon-lacking bulbar dopaminergic neurons and neighbouring excitatory neurons remained unchanged. Within the same sensory circuits, specific cell types can therefore make distinct plastic changes in response to an ever-changing external landscape.

INTRODUCTION

One way that animals can ensure appropriate behavioural choices when faced with an ever-changing environment is to alter the way they process sensory inputs. To implement such adaptive control at the level of neuronal networks, there exists a huge range of cellular mechanisms of neuronal plasticity. These include structural changes in neuronal morphology, functional changes of synaptic strength, and/or modulation of intrinsic excitability (Brzosko et al., 2019; Citri and Malenka, 2008; Debanne et al., 2019; Kullmann et al., 2012; Roy et al., 2020; Wefelmeyer et al., 2016). This extensive repertoire also includes a form of structural plasticity tightly linked with changes in neuronal excitability: plasticity of the axon initial segment (AIS).

Structurally, the AIS is a subcellular zone located in the proximal portion of the axon, where an intricate arrangement of cytoskeletal and scaffolding proteins anchors a membrane-bound collection of signaling molecules, receptors and ion channels (Hamdan et al., 2020; Leterrier, 2018; Vassilopoulos et al., 2019). Functionally, the AIS serves two key roles: maintenance of dendritic/axonal polarity (Hedstrom et al., 2008), and initiation of action potentials (Bean, 2007; Kole et al., 2007). Plastically, the AIS has been proven capable of changing its structure in terms of length, distance from the soma, and/or molecular content (Ding et al., 2018; Grubb and Burrone, 2010; Kuba et al., 2010, 2015; Lezmy et al., 2017).

How is AIS plasticity driven by changes in neuronal activity? *In vitro*, elevated activity can cause the AIS of excitatory neurons to relocate distally or to decrease in length, structural changes that are usually associated with decreased functional excitability (Chand et al., 2015; Evans et al., 2013, 2015; Grubb and Burrone, 2010; Horschitz et al., 2015; Lezmy et al., 2017; Muir and Kittler, 2014; Sohn et al., 2019; Wefelmeyer et al., 2015). *In vivo*, activity-dependent structural AIS plasticity has been observed in excitatory neurons, usually induced by manipulations that are long in duration and/or involve damage to peripheral sensory organs (Akter et al., 2020; Gutzmann et al., 2014; Kuba et al.,

2010; Pan-Vazquez et al., 2020), but see (Jamann et al., 2020)). But is AIS plasticity a prerogative of excitatory neurons, or is it also included in the plasticity toolkit of inhibitory cells? We previously found that, *in vitro*, inhibitory dopaminergic (DA) interneurons in the olfactory bulb (OB) are capable of bidirectional AIS plasticity, inverted in sign with respect to their excitatory counterparts: their AIS increases in length and relocates proximally in response to chronic depolarization, and shortens when spontaneous activity is silenced (Chand et al., 2015). Taken together, these studies begin to paint a picture of how different cell types respond to changes in incoming activity levels by initiating distinct plastic structural changes at their AIS. However, many key questions remain unanswered. Are more physiological, minimally-invasive sensory manipulations sufficient to induce AIS plasticity *in vivo*? In the intact animal, can AIS plasticity occur over more rapid timescales? And do excitatory and inhibitory neurons in sensory circuits respond to such brief and naturally-relevant sensory manipulation with similar levels of AIS plasticity?

To address these questions, we interrogated circuitry in the mouse OB responsible for the earliest steps in odour processing (Shepherd, 2005). At just one synapse away from the sensory periphery, activity in the OB can be readily and reliably altered by physiologically-relevant alterations in sensory experience (Coppola, 2012). In our case this was achieved by unilaterally plugging a nostril for just one day, a minimally-invasive manipulation which effectively mimics the sensory disturbance associated with common respiratory infections, without damaging the olfactory sensory epithelium (Fokkens et al., 2012). We found that such brief sensory deprivation produced structural and functional intrinsic plasticity in axon-bearing dopaminergic (DA) neurons in the bulb's glomerular layer (Chand et al., 2015; Galliano et al., 2018). By targeting excitability in one specialised dopaminergic subpopulation, experience-dependent plasticity in early olfactory networks might act to fine-tune sensory processing in the face of continually fluctuating inputs.

MATERIALS AND METHODS

Animals

We used mice of either sex, and housed them under a 12-h light-dark cycle in an environmentally controlled room with free access to water and food. Wild-type C57BL/6 mice (Charles River) were used either as experimental animals, or to back-cross each generation of transgenic animals. The founders of our transgenic mouse lines – DAT^{IREScre} (B6.SJL-*Slc6a3*$^{tm1.1(cre)Bkmn}$/J, Jax stock 006660) and Ai9 (B6.Cg–*Gt(ROSA)26Sor*$^{tm9(CAG-tdTomato)Hze}$/J; Jax stock 007909) were purchased from Jackson Laboratories. All experiments were performed between postnatal days (P) 21 and 35. All experiments were performed at King's College London under the auspices of UK Home Office personal and project licences held by the authors.

Sensory manipulation

To perform unilateral naris occlusion, mice were briefly anaesthetized (<5 min) with isoflurane. In the occluded group, a custom-made ~5 mm Vaseline-lubricated plug, constructed by knotting suture (Ethilon polymide size 6, non-absorbable suture, Ethicon, UK) around a piece of unscented dental floss and pulled through the lumen of PTFE-tubing with an outer-diameter of 0.6 mm and inner-diameter of 0.3 mm (VWR International, cat#: S1810-04; see (Cummings et al., 2014)) was inserted into the right nostril where it remained for 24 hours. Only the right olfactory bulb was then used for experiments. At the termination of each experiment, post-hoc visual observation of the nasal cavity was always performed to ensure that the plug had remained in place. The few mice where the plug could not be found were not used for experiments. All control animals were gender and age-matched mice left unperturbed in their home cage. For both control and occluded groups, only right bulbs were analysed.

Immunohistochemistry

Mice were anesthetized with an overdose of pentobarbital and then perfused with 20 mL PBS with

heparin (20 units.mL^{-1}), followed by 20mL of 1% paraformaldehyde (PFA; TAAB Laboratories; in 3% sucrose, 60 mM PIPES, 25 mM HEPES, 5 mM EGTA, and 1 mM $MgCl_2$; this relatively weak fixative solution facilitates staining for AIS-localised proteins, especially ankyrin-G).

To expose the olfactory epithelia the rostral half of the calvaria (anterior to the bregma) and the nasal bone were removed, and the samples were first post-fixed overnight (4°C) and then placed in 0.25 M EDTA (Invitrogen AM9261) in PBS at 4°C for 3 days for decalcification. After overnight cryoprotective treatment with 30% sucrose (Sigma S9378), they were then embedded in OCT (VWR Chemicals 00411243), frozen in liquid nitrogen and sliced on a cryostat (Leica CM 1950) into 20 µm slices.

The olfactory bulbs were dissected and post-fixed in 1% PFA for 2-7 days, then embedded in 5% agarose and sliced at 50 µm using a vibratome (VT1000S, Leica). For experiments which aimed at comparing intensity of staining across mice, we co-embedded the bulbs of one control and one occluded mouse in a large agarose block ("set"), and from then forward we processed them as a unit (Vlug et al., 2005). To assess the suitability of the co-embedding strategy and the variability of staining intensity between unperturbed animals, a subset of OBs from control mice were processed together: in the same agarose block, the right and left OB from one control mouse (mouse #1) were co-embedded with the right OB from a second control mouse (mouse #2).

Free-floating slices or sets were washed with PBS and incubated in 5% normal goat serum (NGS) in PBS/Triton/azide (0.25% triton, 0.02% azide) for 2 h at room temperature. They were then incubated in primary antibody solution (in PBS/Triton/azide; Table 1) for 2 days at 4°C.

Slices were then washed three times for 5 min with PBS, before being incubated in secondary antibody solution (species-appropriate Life Technologies Alexa Fluor®; 1:1000 in PBS/Triton/azide) for

3 h at room temperature. After washing in PBS, slices were either directly mounted on glass slides, Menzel-Gläser) with MOWIOL-488 (Calbiochem), or first underwent additional counterstaining steps with NucRed Live 647 (Invitrogen R37106) at room temperature for 25 min to visualize cell nuclei, or with 0.2% Sudan black in 70% ethanol at room temperature for 3 min to minimize autofluorescence. Unless stated otherwise all reagents were purchased from Sigma.

Fixed-tissue imaging and analysis

All images were acquired with a laser scanning confocal microscope (Zeiss LSM 710) using appropriate excitation and emission filters, a pinhole of 1 AU and a 40x oil immersion objective. Laser power and gain were set to either prevent signal saturation in channels imaged for localisation analyses, or to permit clear delineation of neuronal processes in channels imaged for neurite identification (*e.g.*, TH, SMI-32, CCK). All quantitative analysis was performed with Fiji (Image J) by experimenters blind to group identity.

For olfactory epithelium (OE) analysis, 4 images were acquired from consistently positioned septal and dorsomedial regions of interest within each section, with a 1x zoom (0.415 µm/pixel), 512x512 pixels, and in z-stacks with 1 µm steps. OE thickness was measured on single plane images by drawing a straight line, parallel to olfactory sensory neurons (OSNs) dendrites, from the lamina propria to the tips of the OSN dendrites (visualized with OMP label). OSN density was calculated on single-plane image by counting the number of clearly OMP-positive somas (OMP label surrounding NucRed+ nucleus), divided by length of OE in that image, x100 for comparative purposes (Cheetham et al., 2016; Kikuta et al., 2015). To quantify cell apoptosis, expressed as cells/mm for comparative purposes, the number of Caspase-3-positive cells was measured from Z-stacks through entire slice, and then divided by total length of the OE in the stack (OE length x n of z steps) (Kikuta et al., 2015).

For activity early genes and TH expression in the olfactory bulb, images were taken with a 1x zoom

(0.415 µm/pixel), 512x512 pixels, and in z-stacks with 1 µm steps, with identical laser power and digital gain/offset settings within each set. In all animals, images were sampled from the rostral third, middle third, and caudal third of the OB. To avoid selection biases, all cells present in the stack and positive for the identifying marker (TH or SMI-32) were measured. DA cell density was calculated for each image by dividing the number of analysed TH-positive cells by the volume of the glomerular layer (z depth x glomerular layer area, drawn and measured in a maximum intensity projection of the TH channel). SMI-32 positive M/TCs were selected by position in the mitral layer; SMI-32 positive ETCs were included in the analysis only if their soma bordered with both the GL and external plexiform layer. TH positive DA cells were included in the analysis only if their soma was in or bordering with the glomerular layer. Soma area was measured at the single plane including the cell's maximum diameter by drawing a region of interest (ROI) with the free-hand drawing tool. Within each co-embedded set, the staining intensity of each ROI (expressed as mean grey value) was normalized to the mean value of staining intensity across all measured cells in the control slice. For analyses of within- versus between-mouse staining variability, the mean grey value of each M/TC ps6 ROI was normalized to the mean value across all measured cells in the right-OB slice from mouse #1. Mean normalized intensities were then calculated for each slice, and absolute differences in these mean intensities were taken between the left- and right-bulb slices from mouse #1 (for intra-animal variation), and between the slice from the mouse #2 and both left- and right-bulb slices from mouse #1. These two separate between-mouse differences were averaged to give an overall estimate of inter-animal variation, which was compared with intra-animal variation on a slide-by-slide basis in a paired design. Staining intensity in AIS-positive DA cells (*i.e.,* AnkG+/TH+) was normalized within each slide (rostral/middle/caudal) of each set, to the average TH or cFos staining of the overall DA cell population in the control slice.

For AIS identification, images were taken with 3x zoom, 512x512 pixels (0.138 µm/pixel) and in z-stacks with 0.45 µm steps. While in all glutamatergic neurons only one extensive AnkG-positive

region could be found on the proximal part of a process originating directly from the soma, DA cells' AISs were found either on processes originating directly from the soma ("soma-origin") or on a process that did not originate directly from the soma ("dendrite-origin"). Moreover, as previously reported in the literature (Kosaka et al., 2008; Meyer and Wahle, 1988) a minority of DA cells was found to carry multiple AISs (10% of all imaged cells) and excluded from further analysis. In all cells carrying a single AIS, its distance from soma and length were measured in Fiji/ImageJ using the View5D plugin, which allows for 3D manual tracing of cell processes. Laser power and gain settings were adjusted to prevent signal saturation in the AIS label AnkG; cellular marker TH or SMI-32 signal was usually saturated to enable clear delineation of the axon. The AIS distance from soma was calculated as the neurite path distance between the start of the AIS (the proximal point where AnkG staining became clearly identifiable) and the intersection of its primary parent process (usually the axon, but in the case of dendrite-origin axons the axon-bearing primary dendrite) with the border of the soma. AIS length was calculated by following AnkG staining along the course of the axon from the AIS start position to the point where AnkG staining was no longer clearly identifiable. To confirm the reliability of this manual tracing method, a subset of 50 AISs was analysed twice by EG, blindly and with two weeks' inter-analysis interval. Measurements of both distance from soma and length were highly consistent between the two analysis sessions (AIS distance from soma: difference mean ± SEM 0.006 ± 0.097 μm, $r^2 = 0.75$; AIS length: difference 0.139 ± 0.195 μm, $r^2 = 0.95$). Relative AnkG mean staining intensity in axon-bearing DA cells was measured by drawing a freehand line along the AIS profile at the single z plane that contained the longest segment of the AIS. This process was repeated for all other AISs present in the same image stack, regardless of cellular origin (*i.e.*, from ETCs and other interneurons), and the average staining intensity per stack was used for normalization.

Acute-slice electrophysiology

P21-35 C57BL/6 or $DAT^{IREScre}$ x Ai9 (DAT-tdTomato) mice were decapitated under isoflurane

anaesthesia and the OB was removed and transferred into ice-cold slicing medium containing (in mM): 240 sucrose, 5 KCl, 1.25 NaH_2PO_4, 2 $MgSO_4$, 1 $CaCl_2$, 26 $NaHCO_3$ and 10 D-Glucose, bubbled with 95% O_2 and 5% CO_2. Horizontal slices (300 µm thick) of the olfactory bulb were cut using a vibratome (VT1000S, Leica) and maintained in ACSF containing (in mM): 124 NaCl, 5 KCl, 1.25 NaH_2PO_4, 2 $MgSO_4$, 2 $CaCl_2$, 26 $NaHCO_3$ and 20 D-Glucose, bubbled with 95% O_2 and 5% CO_2 for >1 h before experiments began.

Whole-cell patch-clamp recordings were performed using a Multiclamp 700B amplifier (Molecular Devices, Union City, CA, USA) at physiologically-relevant temperature (32-34°C) with an in-line heater (TC-344B, Warner Instruments). Signals were digitized (Digidata 1550, Molecular Devices) and Bessel-filtered at 3 KHz (membrane test pulses) or 10 KHz (all other protocols). Test recordings in DAT-tdTomato neurons (n = 3; data not shown) confirmed that varying the Bessel filter between 2 KHz and 30 KHz had no impact on fundamental waveform features around action potential onset; filtering at 10 KHz was therefore not a limiting factor in identifying cell subtypes based on their spike shape (see below). Recordings were excluded if series (RS) or input (RI) resistances (assessed by -10 mV voltage steps following each test pulse, acquisition rate 20 KHz) were respectively higher than 30 MΩ or lower than 100 MΩ for DA neurons, higher than 30 MΩ or lower than 30 MΩ for ETCs, higher than 20 MΩ or lower than 40 MΩ for M/TCs, or if they varied by >20% over the course of the experiment. Fast capacitance was compensated in the on-cell configuration and slow capacitance was compensated after rupture. Cell capacitance (Cm) was calculated by measuring the area under the curve of the transient capacitive current elicited by a -10 mV voltage step. Resting membrane potential (Vm) was assessed immediately after break-in by reading the voltage value in the absence of current injection (I=0 configuration). Recording electrodes (GT100T-10, Harvard Apparatus) were pulled with a vertical puller (PC-10, Narishige) and filled with an intracellular solution containing (in mM): 124 K-Gluconate, 9 KCl, 10 KOH, 4 NaCl, 10 HEPES, 28.5 Sucrose, 4 Na_2ATP, 0.4 Na_3GTP (pH 7.25-7.35; 290 MOsm) and Alexa 488 (1:150). Cells were visualized using an upright microscope

(Axioskop Eclipse FN1 Nikon, Tokyo, Japan) equipped with a 40x water immersion objective, and for DA cell identification tdT fluorescence was revealed by LED (CoolLED pE-100) excitation with appropriate excitation and emission filters (ET575/50m, CAIRN Research, UK). M/TCs were identified based on location in the mitral cell layer and large somas. ETCs were identified based on: (a) location in the lower glomerular layer / upper external plexiform layer; (b) large and balloon-shaped soma and, often, visible large apical dendrite; (c) characteristic spontaneous burst firing when unclamped; (d) an relatively depolarized resting membrane potential of ~-55 mV; and (e) distinct depolarising sag potential when injected with prolonged negative current steps in current clamp mode (Liu and Shipley, 2008; Liu et al., 2013).

In current-clamp mode, evoked spikes were measured with V_{hold} set to −60 ± 3 mV for M/TCs and DA cells, and to −55 ± 3 mV for ETCs. For action potential waveform measures, we injected 10-ms-duration current steps from 0 pA of increasing amplitude (Δ5/20 pA) until we reached the current threshold at which the neuron reliably fired an action potential (V_m > 0 mV; acquisition rate 200 KHz). For multiple spiking measures, we injected 500-ms-duration current steps from 0pA of increasing amplitude (Δ2/10 pA) until the neuron passed its maximum firing frequency (acquisition rate 50 KHz). Exported traces were analysed using either ClampFit (pClamp10, Molecular Devices) or custom-written routines in Matlab (Mathworks). Before differentiation for *dV*/*dt* and associated phase plane plot analyses, recordings at high temporal resolution (5 μs sample interval) were smoothed using a 20 point (100 μs) sliding filter. Voltage threshold was taken as the potential at which *dV*/*dt* first passed 10 V/s. Onset rapidness was taken from the slope of a linear fit to the phase plane plot at voltage threshold. Spike width was measured at the midpoint between voltage threshold and maximum voltage. Rheobase and afterhyperpolarization values were both measured from responses to 500 ms current injection, the latter from the local voltage minimum after the first spike fired at rheobase. Input-output curves were constructed by simply counting the number of spikes fired at each level of injected current.

For DA cells, monophasic versus biphasic phase plane plots were visually determined by EG and MSG. We classified completely monotonic plots with continually increasing rate-of-rise as monophasic, and any plots showing a clear inflection in rate-of-rise over the initial rising phase as biphasic. Any discrepancies in classification were resolved by mutual agreement. We also corroborated our subjective classification using a quantitative measure of spike onset sharpness: the ratio of errors produced by linear and exponential fits to the peri-threshold portion of the phase plane plot (Baranauskas et al., 2010; Volgushev et al., 2008). Fit error ratios were calculated with a custom Matlab script written by Maxim Volgushev, using variable initial portions of the phase plane plot between voltage threshold and 40% of maximum dV/dt (Baranauskas et al., 2010), for single spikes fired in response to 10 ms current injection at current threshold and up to three subsequent suprathreshold sweeps (Galliano et al., 2018). In M/TC recordings, as expected for large projection neurons with a prominent AIS (Volgushev et al., 2008), these fit error ratios were consistently high (mean ± SEM 5.45 ± 0.58 at 20% maximum dV/dt, n = 35), reflecting their markedly sharp spike onset even in the absence of a clearly biphasic phase plane plot profile. In DA cells, we used strict, established (Baranauskas et al., 2010), but non-inclusive criteria for 'steep' (≈ biphasic; maximum fit error ratio >3) versus 'smooth' (≈ monophasic; maximum fit error ratio <1) spike onset. This enabled us to objectively classify phase plane plot shape in a smaller subset (n = 28/48, = 58%) of our recorded DAT-tdTomato neurons. This quantitatively-characterised subset included just 3 cells (= 11%) which were classified differently by our subjective versus objective criteria. Importantly, excluding these differentially-classified cells from our analyses made no difference to any of our results in terms of significance.

Statistical analysis

Statistical analysis was carried out using Prism (Graphpad), SPSS (IBM) or Matlab (Mathworks). Sample distributions were assessed for normality with the D'Agostino and Pearson omnibus test,

and parametric or non-parametric tests carried out accordingly. α values were set to 0.05, and all comparisons were two-tailed. For multilevel analyses, non-normal distributions were rendered normal by logarithmic transform. These parameters were then analysed using linear mixed models (SPSS) with mouse or set as the subject variable (Aarts et al., 2014).

RESULTS

Brief unilateral naris occlusion leaves the olfactory epithelium undamaged

Olfactory sensory deprivation in mice can be achieved surgically by cauterisation of one naris, or mechanically by insertion of a custom-made and removable nasal plug (Coppola, 2012). Traditionally, both methods have been employed for prolonged periods (weeks, months at a time), and are accompanied by pronounced and widespread changes in olfactory bulb architecture, including overall OB size. This scenario is potentially pathological, and does not reflect the most common deprivation that this sensory system has to deal with: a nasal blockage lasting less than 5 days (Fokkens et al., 2012).

In order to induce activity-dependent plasticity within a more naturally-relevant timeframe, we employed the custom-made plug method (Cummings and Brunjes, 1997), but left the plug in place for just one day (Fig. 1A). This 24 h duration is longer than the natural sub-circadian cycles of relative air flow alternation between the nostrils (Bojsen-Moller and Fahrenkrug, 1971; Kahana-Zweig et al., 2016), but is well within the range of common infection-induced nasal blockade (Fokkens et al., 2012). We also chose it because we knew one day of activity manipulation was sufficient to produce multiple forms of plasticity in cultured OB neurons (Chand et al., 2015). Because of concerns regarding abnormal airflow through the remaining open nostril in unilaterally occluded animals (Coppola, 2012; Kass et al., 2013; Wu et al., 2017), we did not compare open and occluded hemispheres within the same experimental animals. Instead, juvenile (P27) wild-type mice were either left unperturbed (Fig. 1A; control group, Ctrl, black) or had one nostril plugged for 24 h (occluded group, Occl, orange), before being perfused and processed for immunohistochemistry.

To confirm the expected lack of peripheral pathology with this approach (Cheetham et al., 2016; Kikuta et al., 2015), we assessed the impact of plug insertion on the olfactory epithelium (OE; Fig. 1B). We found no difference between control and 24 h-occluded groups in overall OE thickness (Fig.

1C; Ctrl mean ± SEM 86.51 ± 2.26 µm, n = 12 sample regions, N = 3 mice; Occl 82.26 ± 2.40 µm n = 12 sample regions, N = 3 mice; mixed model ANOVA nested on mouse, effect of treatment $F_{1,24} = 1.81$, $p = 0.19$). Similarly, the density of mature olfactory sensory neurons (OSNs, identified by immunolabel for olfactory marker protein, OMP) did not differ between control and occluded mice (Fig. 1D; Ctrl mean ± SEM 52.84 ± 5.24 cells/100 µm, n = 12 sample regions, N = 3 mice; Occl 46.20 ± 2.78 cells/100 µm, n = 12 sample regions, N = 3 mice; mixed model ANOVA nested on mouse, effect of treatment $F_{1,6} = 0.584$, $p = 0.47$), nor did the density of apoptotic cells positive for activated Caspase-3 (Fig. 1E; Ctrl mean ± SEM 0.39 ± 0.084 cells/mm, n = 12 sample regions, N = 3 mice; Occl 0.29 ± 0.094 cells/mm, n = 12 sample regions, N = 3 mice; mixed model ANOVA nested on mouse, effect of treatment $F_{1,6} = 0.423$, $p = 0.54$). Overall, these data suggest that brief olfactory deprivation carried out with a custom-made plug has no impact on the overall structure and health of the olfactory epithelium.

Brief unilateral naris occlusion alters the activity of inhibitory and excitatory bulbar neurons

Given that our chosen sensory manipulation is well within naturally-experienced timeframes (Fokkens et al., 2012) and does not overtly damage the peripheral sense organ, we next checked that it was effective in reducing ongoing activity levels in downstream OB neurons.

We processed the OBs of control and occluded mice to quantify the expression of activity markers with immunohistochemistry. To control for differences in antibody exposure, we co-embedded slices from control and occluded mice in agarose blocks ("sets", Fig. 2A) for consistent histological processing, and normalized activity marker intensity within each set (see Materials and Methods). We confirmed that this approach was effective in reducing inter-animal staining variability by analyzing a separate group of co-embedded sets which each contained slices from both the left and right OB of one unperturbed control mouse (allowing comparison of within-mouse variation between the two bulbs), plus an OB slice from a second unperturbed control mouse (allowing

371 comparison of between-mouse variation; see Materials and Methods). In these analyses of tissue
372 that all came from the same treatment group, we found that within-mouse absolute differences in
373 mean staining intensity were not significantly different from between-mouse differences (paired t-
374 test, $t_8 = 1.02$, $n = 9$ slides, $p = 0.34$), suggesting that our approach of slice co-embedding and
375 standardized histological processing was sufficiently effective to reduce inter-animal variation down
376 to the level of intra-animal variation.
377
378 We first analysed the expression of the immediate early gene cFos (Barnes et al., 2015) in
379 dopaminergic inhibitory neurons (DA cells, identified via tyrosine hydroxylase, TH, immunoreactivity;
380 Fig. 2B). DA cells in occluded bulbs displayed markedly and consistently lower spontaneous activity-
381 related cFos levels than their co-embedded control counterparts, and this effect was highly
382 significant in multilevel statistical analyses that account for inter-set variation (Fig. 2B; Ctrl
383 mean ± SEM 1 ± 0.02, n = 369 cells, N = 3 sets; Occl 0.56 ± 0.02, n = 301 cells, N = 3 sets; mixed model
384 ANOVA nested on set, effect of treatment $F_{1,667} = 233$, $p < 0.0001$).
385
386 Previous work from ourselves and others has found that bulbar DA neurons are a heterogeneous
387 population (Chand et al., 2015; Galliano et al., 2018; Korshunov et al., 2020; Kosaka et al., 2019).
388 Two non-overlapping subtypes can be identified by a spectrum of different morphological and
389 functional characteristics, as well as by a binary classifier: the presence or absence of an axon and its
390 key component, the axon initial segment (AIS) (Chand et al., 2015; Galliano et al., 2018). So, does
391 brief unilateral naris occlusion downregulate activity in both axon-bearing and anaxonic DA
392 subtypes? Soma size is a readily-obtainable proxy indicator for DA subtypes: anaxonic DA cells are
393 usually small, while axon-bearing DA cells tend to have very large somas. Using previously defined
394 lower (<70 μm^2) and upper (>99μm^2) bounds of the OB DA soma size distribution (Galliano et al.,
395 2018), we found that both small/putative anaxonic DA cells and large/putative axon-bearing DA cells
396 from occluded mice display reduced cFos staining relative to their co-embedded control

counterparts. Although the smaller sample size of the much rarer large DA cells accentuated variability across staining sets here, this effect was highly significant for both cell types in analyses that specifically account for that variation (small cells: Ctrl mean ± SEM 0.99 ± 0.03, n = 298 cells from N = 3 sets; Occl 0.56 ± 0.02, n = 192 cells, N = 3 sets; mixed model ANOVA nested on mouse, effect of treatment $F_{1,489} = 166$, $p < 0.0001$; big cells: Ctrl mean ± SEM 1.11 ± 0.11, n = 22 cells from N = 3 sets; Occl 0.67 ± 0.07, n = 33 cells, N = 3 sets; mixed model ANOVA nested on mouse, effect of treatment, $F_{1,53} = 11.91$, $p < 0.0001$). Finally, to further confirm these results in DA cells which definitively belonged to the axon-bearing subtype, we co-stained a subset of tissue with the AIS marker ankyrin-G (AnkG) and measured cFos levels in AnkG+/TH+ DA cells (Fig. 2F; see Materials and Methods). Once more, we found significantly dimmer cFos fluorescence in occluded cells (Fig. 2G; Ctrl mean ± SEM 1.28 ± 0.10, n = 14 cells, Occl 0.95 ± 0.09, n = 22 cells, Mann-Whitney, U = 82, p = 0.02).

This effect of naris occlusion on activity levels was more variable, but nevertheless also present overall in bulbar glutamatergic neurons. These belong to two main classes defined by location and axonal projections: mitral/tufted cells and external tufted cells. Mitral/tufted cells (M/TCs, Fig. 3A), whose soma sits in the mitral cell layer, are the bulbar network's principal neurons; they extend their apical dendrites to the glomerular layer where they receive direct and indirect inputs from OSNs, and send their axons to higher olfactory areas, including piriform cortex (Imai, 2014). External tufted cells (ETCs, Fig. 3C) are glutamatergic interneurons located in the glomerular layer, where they provide local dendrodendritic amplification of sensory inputs (Gire et al., 2012; Najac et al., 2011). ETC axons do not leave the OB, but target deep-layer networks beneath sister glomeruli in the opposite hemi-bulb (Cummings and Belluscio, 2010; Lodovichi et al., 2003). To identify both classes of excitatory neurons, we labelled bulbar slices with the neurofilament marker protein H, clone SMI-32 (Table 1).

We co-stained with antibodies against another activity marker, phospho-S6 ribosomal protein (pS6; Knight et al., 2012) which in bulbar glutamatergic cells gives higher intensity and consistency of staining than cFos (Fig. 3A,C). Using a co-embedding approach to allow comparisons of relative staining intensity across slices (Fig. 2A; see Materials and Methods), we found that in both M/TCs and ETCs from occluded slices, the relative intensity levels of pS6 were markedly variable across staining sets (see set-by-set comparisons in Fig. 3B,D). This may be due to cell- and/or marker-type differences in activity changes occurring during brief sensory deprivation. Mouse-to-mouse differences in the efficacy of naris block may also play a role here, although the more consistent effects of occlusion on cFos staining in DA cells (Fig. 2C; see also Byrne et al., 2020) suggest this is not a strong contributing factor. To account for the considerable set-to-set variability in our ps6 data, we used multilevel statistical analyses with our cell-by-cell data nested by co-embedded set (Aarts et al., 2014), finding that pS6 intensity was significantly decreased overall in both cell types in occluded bulbs when compared to co-embedded controls (M/TC Ctrl mean ± SEM 1.00 ± 0.013, n = 858 cells; Occl 0.80 ± 0.015, n = 930 cells, N = 6 sets; mixed model ANOVA nested on set, effect of treatment, $F_{1,1783} = 94$, $p < 0.0001$; Fig. 3B; ETC Ctrl 1.00 ± 0.012, n = 642 cells; Occl 0.89 ± 0.018, n = 624 cells, N = 6 sets; mixed model ANOVA nested on set, effect of treatment, $F_{1,1264} = 22$ $p < 0.0001$; Fig. 3D).

In summary, despite some mouse-to-mouse variability which is more marked for excitatory neurons, short-duration naris occlusion comparable to the sensory deprivation produced by a mild common cold (Fokkens et al., 2012), is effective overall in reducing activity levels in multiple OB cell types.

Lack of structural and intrinsic activity-dependent plasticity in excitatory neurons

Previous *in vitro* work from our laboratory has demonstrated that both GABAergic and GABA-negative neurons in bulbar dissociated cultures respond to 24 h manipulations of neuronal activity by modulating the length and/or position of their AIS (Chand et al., 2015). This finding raised a number of questions, namely, (a) whether AIS plasticity also occurs *in vivo* in response to a sensory

449 manipulation of similar duration, (b) if so, in which cell types, and, finally (c) whether structural
450 plasticity at the AIS is accompanied by functional plasticity of the neurons' intrinsic excitability.
451
452 In multiple cell types after 24 h naris occlusion, we performed *ex vivo* immunohistochemistry to
453 quantify AIS position and length, and whole-cell patch clamp recording in acute slices to assess
454 neurons' passive and active electrophysiological properties.
455
456 In fixed slices of juvenile C57BL/6 mice, we identified M/TCs by staining the neurofilament protein H,
457 clone SMI-32 (Ashwell, 2006). AISs were identified with staining against ankyrin-G (AnkG, Fig. 4A),
458 and measured in 3D (see Materials and Methods). M/TCs all have a prominent and reliably-oriented
459 axon which arises directly from the soma and projects towards the granule cell layer of the OB.
460 Their AnkG-positive AISs tend to be ~25 μm in length and proximally located (Lorincz and Nusser,
461 2008).
462
463 We found no difference in AIS distance from the soma (Ctrl mean ± SEM, 2.92 ± 0.21 μm, n = 61
464 cells, N = 3 mice; Occl, 3.25 ± 0.15 μm, n = 87 cells, N = 4 mice; mixed model ANOVA of log-
465 transformed AIS distance nested on mouse, effect of treatment, $F_{1,6} = 1.24$, $p = 0.31$), nor in AIS
466 length (Ctrl, mean ± SEM 26.17 ± 0.58 mm; Occl, 25.91 ± 0.40 mm; mixed model ANOVA nested on
467 mouse, effect of treatment $F_{1,8} = 0.24$, $p = 0.64$) between control and occluded M/TCs (Fig. 4B-D).
468 This lack of structural AIS plasticity was mirrored by an equal absence of plastic changes in M/TCs'
469 intrinsic excitability. When probed with short current injections (10 ms, Fig. 4F left), control and
470 occluded M/TCs fired an action potential at similar thresholds, both in terms of injected current (Fig.
471 4G; Ctrl, mean ± SEM, 323 ± 45 pA, n = 16 cells; Occl, 317 ± 36 pA, n = 23 cells; unpaired t-test,
472 $t_{37} = 0.098$, $p = 0.92$) and somatic membrane voltage (Fig. 4H; Ctrl, mean ± SEM -39.86 ± 0.67 mV,
473 n = 16 cells; Occl, -37.80 ± 0.83 mV, n = 23 cells; Mann-Whitney test, U = 121, p = 0.07). These
474 threshold single spikes in M/TCs were characterised by their markedly sharp onset – particularly

clear in their spike phase-plane plots (Fig. 4F left insets) – consistent with action potential initiation away from the recording site, presumably in the AIS (see Materials and Methods)(Bean, 2007; Bender and Trussell, 2012; Coombs et al., 1957; Foust et al., 2010; Jenerick, 1963; Khaliq et al., 2003; Kole et al., 2007; Shu et al., 2007). When probed with longer 500 ms current injections to elicit repetitive action potential firing (Fig. 4F left), we again found no difference between the two groups (Fig. 4I; Ctrl n = 16 cells, Occl, n = 23 cells; mixed-model ANOVA, effect of treatment, $F_{1,51} = 0.30$, p = 0.59). Moreover, control and occluded M/TCs did not differ significantly in any other measured electrophysiological property, passive or active (Table 2).

Similarly, we also found no evidence for structural or intrinsic activity-dependent plasticity in ETCs. In these experiments we visualized ETCs in fixed tissue by staining for cholecystokinin (CCK, Fig. 4A; (Liu and Shipley, 1994)). We found that, as for M/TCs, ETC AISs are prominent AnkG-positive segments located quite proximally on a process originating directly from the soma. These AISs were equally distant from the soma (Fig. 5C; Ctrl mean ± SEM, 2.67 ± 0.23 μm, n = 65 cells, N = 3 mice; Occl, 2.496 ± 0.22 μm, n = 62 cells, N = 3 mice; mixed model ANOVA of log-transformed AIS distance nested on mouse, effect of treatment, $F_{1,6} = 0.018$, p = 0.90) and equally long (Fig. 5D; Ctrl mean ± SEM, 18.52 ± 0.39 μm, n = 65 cells, N = 3 mice; Occl, 19.94 ± 0.59 μm, n = 62 cells, N = 3 mice; mixed model ANOVA nested on mouse, effect of treatment, $F_{1,6} = 2.31$, p = 0.18) in control and occluded mice. Moreover, when probed electrophysiologically in acute slices (Fig. 5F-G; Table 3), ETCs from control and occluded mice fired sharp-onset single action potentials at similar thresholds (current threshold, Fig. 5G, Ctrl mean ± SEM, 103 ± 8 pA, n = 35 cells; Occl, 112 ± 7 pA, n = 57 cells, Mann-Whitney test, U = 913, p = 0.50; voltage threshold, Fig. 5H, Ctrl -39.10 ± 0.48 mV, n = 35 cells; Occl -38.56 ± 0.48 mV, n = 57 cells; Mann-Whitney test, U = 926, p = 0.57), and similarly modulated their repetitive firing in response to long current injections of increasing intensity (Fig. 5I; Ctrl n = 30 cells, Occl n = 45 cells; mixed-model ANOVA, effect of treatment, $F_{1,96} = 1.80$, p = 0.18).

Taken together, these results confirm that while both major classes of bulbar excitatory neurons experience an overall drop in activity after 24 h sensory deprivation (Fig. 2), they do not respond by altering the structural features of their AIS or their intrinsic physiological properties.

Both inhibitory dopaminergic neuron subclasses downregulate their TH expression levels in response to brief naris occlusion

In other brain areas inhibitory interneurons can act as first responders in the early phases of adaptation to changed incoming activity, plastically changing their overall structure and function to maintain circuit homeostasis (Gainey and Feldman, 2017; Hartmann et al., 2008; Keck et al., 2017; Knott et al., 2002; Yin and Yuan, 2014). Given the lack of plasticity in glutamatergic OB neurons following brief 24 h naris occlusion, we reasoned that plastic responses might therefore be more evident in OB inhibitory interneurons. Because of their well-documented plasticity *in vivo* and their ability to undergo activity-dependent AIS changes *in vitro* (Bonzano et al., 2016; Chand et al., 2015), we focused on the bulb's DA population to address this question.

Bulbar DA neurons are unique amongst other glomerular layer inhibitory neurons because of their well-described plasticity in neurotransmitter-synthesising enzyme expression. Changes in sensory input, including those induced by unilateral naris occlusion, are known to produce alterations in tyrosine hydroxylase (TH) expression at both the protein and mRNA levels (Baker et al., 1993; Cummings and Brunjes, 1997; Kosaka et al., 1987; Nadi et al., 1981). As with other forms of experience-dependent plasticity, these changes have been mostly investigated using long-duration manipulations. However, 2 days of deprivation were reported to induce a small, but significant, decrease in whole-bulb *Th* mRNA (Cho et al., 1996), whilst just one day of elevated activity was sufficient to increase TH immunofluorescence intensity or TH-GFP transgene expression, respectively, in dissociated and slice culture preparations (Akiba et al., 2007; Chand et al., 2015). We therefore set out to assess whether 24 h naris occlusion is sufficient to produce activity-dependent

changes in TH expression *in vivo*, and if so whether these changes are observed in both axon-bearing and anaxonic OB DA subtypes.

In three sets of co-embedded control and occluded coronal bulbar slices (Fig. 2B) stained with an antibody against TH (Fig. 6A), we first confirmed that the overall density of labelled DA cells was unaffected by brief sensory deprivation (Fig. 6B; Ctrl mean ± SEM 42317 ± 3661 cells/mm^3, n = 14 regions, N = 3 sets, Occl 39993 ± 4243 cells/mm^3, n = 15 regions, N = 3 sets; mixed model ANOVA nested on set, effect of treatment, $F_{1,25} = 0.39$, $p = 0.54$). In the knowledge that we were labelling a similar number of TH-positive cells in both groups, we then analysed relative TH immunofluorescence levels in each set, normalizing the intensity of staining to average control values (see Materials and Methods). Given the inter-set variability noted in our cFos data (Fig. 2), it was unsurprising to also observe such variability in relative TH intensity levels. This was particularly evident in the smaller occlusion effect observed in set 3 here, and especially for the smaller sample of much rarer large neurons (Fig. 6C-E). We saw similar set-to-set variability in a separate analysis of TH immunofluorescence changes after 24 h occlusion (Byrne et al., 2020) but less variability in whole-bulb qPCR estimates of relative *Th* mRNA levels in that study. This suggests that set-to-set variation in relative TH staining intensity may be driven more by differences in locally imaged regions for immunofluorescence quantification, differences in staining between preparations, and/or more variable occlusion effects at the protein versus transcript level, rather than by mouse-to-mouse differences in the efficacy of naris block. Regardless of the causes of set-to-set variation, multilevel analyses that specifically take it into account revealed highly significant overall reductions in TH immunofluorescence levels in all DA cell groups – significant changes were observed in all DA cells (Fig. 6C; Ctrl mean ± SEM 1.00 ± 0.019 n = 369 cells, N = 3 sets; Occl 0.59 ± 0.023, n = 301 cells, N = 3 sets; mixed model ANOVA nested on set, effect of treatment $F_{1,667} = 212$, $p < 0.0001$), small putative anaxonic cells (Fig. 6D; Ctrl mean ± SEM 1.01 ± 0.02 n = 298 cells, N = 3 sets; Occl 0.64 ± 0.03, n = 192 cells, N = 3 sets; mixed model ANOVA nested on set, effect of treatment $F_{1,489} = 130$, $p < 0.0001$), and

large putative axonal cells (Fig. 6E; Ctrl mean ± SEM 1.01 ± 0.07 n = 22 cells, N = 3 sets; Occl 0.51 ± 0.08, n = 33 cells, N = 3 sets; mixed model ANOVA nested on set, effect of treatment $F_{1,53} = 19$, $p < 0.0001$). We further confirmed this latter phenotype in a smaller subset of DA cells with definitively identified AISs (Fig. 6F; normalized TH intensity; Ctrl mean ± SEM 1.79 ± 0.13, n = 14, Occl 1.37 ± 0.14, n = 22, unpaired t–test, $t_{34} = 2.03$; $p = 0.0498$). We also found significant positive correlations between normalized TH and normalized cFos (Fig. 2) intensities for all groups. These were stronger for control neurons (norm TH vs. norm cFos, Ctrl small cells Pearson r = 0.70, n = 298 cells, $p < 0.0001$; big cells r = 0.89, n = 22, $p < 0.0001$; Occl small cells r = 0.52, n = 192, $p < 0.0001$; big cells r = 0.42, n = 33, $p = 0.015$), suggesting that the mechanisms leading to activity-dependent TH and cFos changes in individual OB DA neurons are only loosely coupled. Overall, given that alterations in OB TH levels are often used to confirm the effectiveness of olfactory sensory manipulations (Cockerham et al., 2009; Grier et al., 2016; Kass et al., 2013), these data supplement the immediate early gene analysis (Fig. 2) to show that 24 h naris occlusion strongly and reliably downregulates activity in both subclasses of OB DA interneurons. They also provide evidence for, to date, the fastest activity-dependent TH change observed in this cell class *in vivo* (see also Byrne et al., 2020).

Anaxonic DA neurons do not modulate their intrinsic excitably following brief sensory deprivation

The vast majority of DA neurons are anaxonic cells (Galliano et al., 2018), which by locally releasing GABA and dopamine in the glomerular layer help to control the overall gain of OSN→M/TC transmission (McGann, 2013; Vaaga et al., 2017). Highly plastic, they retain the capability to regenerate throughout life (Bonzano et al., 2016; De Marchis et al., 2007; Galliano et al., 2018; Lledo et al., 2006). However, although they regulate their levels of TH expression in response to 24 h naris occlusion (Fig. 6), we found that the same manipulation did not change their intrinsic excitability.

We performed whole-cell patch clamp recordings in control and occluded DAT-tdTomato mice (Bäckman et al., 2006; Madisen et al., 2010). This transgenic labelling approach produces red fluorescent tdT-positive glomerular layer cells that are ~75-85% co-labelled for TH (Fig. 7A; (Byrne et al., 2020; Galliano et al., 2018; Vaaga et al., 2017)). The remaining tdT-positive/TH-negative non-dopaminergic labelled OB neurons in these mice are of the calretinin-expressing OB interneuron class and can be readily identified by their unique physiological properties (Byrne et al., 2020; Pignatelli et al., 2005; Sanz Diez et al., 2019), so these were excluded from our analyses. Anaxonic DA cells, which are over-represented in DAT-tdTomato mice (Galliano et al., 2018), were functionally classified by assessing the nature of their action potential phase plane plot of single spikes fired in response to 10 ms somatic current injection (Fig. 7B). A smooth, monophasic phase plane plot is indicative of AP initiation at the somatic recording site, and can be used as a proxy indicator of anaxonic morphology. In contrast, a distinctive biphasic phase plane plot waveform indicates that the AP initiated at a non-somatic location – usually the AIS – and can be used as a proxy for axon-bearing identity (see Materials and Methods)(Bean, 2007; Bender and Trussell, 2012; Chand et al., 2015; Coombs et al., 1957; Foust et al., 2010; Galliano et al., 2018; Jenerick, 1963; Khaliq et al., 2003; Kole et al., 2007; Shu et al., 2007; Werginz et al., 2020). Indeed, we confirmed that monophasic, putative anaxonic cells had smaller soma sizes than putative axon-bearing neurons with biphasic phase plane plot signatures (see below; monophasic mean ± SEM $56.36 \pm 3.40\ \mu m^2$, $n = 25$ cells; biphasic $89.44 \pm 5.19\ \mu m^2$, $n = 21$ cells; unpaired t-test, $t_{44} = 5.49$, $p < 0.0001$)(Chand et al., 2015; Galliano et al., 2018).

We found that, while sitting at a more depolarized resting membrane potential than their control counterparts, monophasic/putative-anaxonic DA cells from occluded mice showed no other significant differences in their passive membrane properties (Table 4). Measures of intrinsic excitability – importantly measured from identical baseline voltage – were indistinguishable between the two groups. Control and occluded monophasic neurons fired single spikes at similar

thresholds (current threshold, Fig. 7D; Ctrl mean ± SEM, 129.7 ± 19.2 pA, n = 13 cells; Occl, 160 ± 29.23 pA, n = 11 cells; unpaired t-test, $t_{22} = 0.89$, p = 0.38; voltage threshold, Fig. 7D; Ctrl -30.47 ± 1.09 mV, n = 13 cells; Occl -30.70 ± 1.37 mV, n = 11 cells; Mann-Whitney test, U = 68, p = 0.86), and, when probed with longer current injections of increasing intensity, fired similar numbers of action potentials (Fig. 7E; mixed model ANOVA, effect of treatment $F_{1,30} = 1.65$, p = 0.21).

Overall, in putative anaxonic/monophasic DA cells the decreases in c-fos and TH expression observed after 24 h naris occlusion are not accompanied by any significant alterations in intrinsic excitability.

DA cells equipped with an axon shorten their axon initial segment and decrease their intrinsic excitability in response to 24 h naris occlusion

Far less abundant than their anaxonic neighbours, axon-bearing DA neurons tend to have a large soma, and dendrites that branch more widely within the glomerular layer (Galliano et al., 2018). Similarly to anaxonic DA cells, they respond to 24 h naris occlusion by decreasing cFos and TH expression (Figs. 3 and 6), but they lack a key characteristic of the former: the dramatic whole-cell structural plasticity which is the ability to regenerate throughout life. Instead of undergoing lifelong neurogenesis, axon-bearing OB DA cells are exclusively born during early embryonic stages (Galliano et al., 2018). However, we have previously shown that, *in vitro*, this DA subtype can undergo a much subtler type of structural plasticity in the form of AIS alterations. In particular, 24 h reduced activity in the presence of tetrodotoxin was associated with decreased AIS length in this cell type (Chand et al., 2015). We therefore set out to investigate whether similar AIS plasticity also occurs *in vivo* in response to the same duration of sensory deprivation.

As for AIS analysis in excitatory neurons, we performed immunohistochemistry in fixed slices of juvenile C57BL/6 mice, double stained for TH to identify DA neurons and ankyrin-G to measure AISs

(AnkG, Fig. 8A). A current leitmotiv in the biology of DA neurons is their striking heterogeneity (Chand et al., 2015; Henny et al., 2012; Kosaka et al., 2019; Morales and Margolis, 2017; Romanov et al., 2017; Zhang et al., 2007), and in OB DA cells here this was also evident in the structure and location of their AIS. We found that OB AISs are of reasonably consistent length (coefficient of variation, CV = 0.34 in control cells), but can be situated at highly variable distances from the soma (control CV = 0.75). Contrary to findings in midbrain DA cells (González-Cabrera et al., 2017; Meza et al., 2018) and in OB dissociated cultures (Chand et al., 2015) we found no consistent relationship between these parameters in bulbar DA neurons (Spearman coefficient of AIS length vs soma distance: Ctrl r = 0.03, n = 68 cells, p = 0.78; Occl, r = 0.04, n = 80 cells, p = 0.73). We also noted that the AIS of an OB DA neuron can be located either on a process that directly emanates from the soma ("soma-origin" AIS), or on a process separated from the soma by one or more branch nodes ("dendrite-origin" AIS; Fig. 8A-B)(González-Cabrera et al., 2017; Höfflin et al., 2017; Houston et al., 2017; Kosaka et al., 2019; Thome et al., 2014; Yang et al., 2019). While this peculiar axonal arrangement challenges the traditional view on neuronal input-output transformation (Kaifosh and Losonczy, 2014), it is not unique to bulbar DA neurons. Indeed, midbrain DA neurons have been shown to carry "dendrite-origin" AISs (González-Cabrera et al., 2017; Yang et al., 2019), and recently the overall variability in AIS length and location in these neurons has been proposed to play a key role in the maintenance of an appropriate pacemaking rhythm in the context of variable dendritic branching (Moubarak et al., 2019). Moreover, "dendrite-origin" AISs are not exclusive to DA neurons: common in invertebrates (Triarhou, 2014), they have also been described in cat and mouse cortex (Hamada et al., 2016; Höfflin et al., 2017; Meyer and Wahle, 1988), in hippocampal pyramidal cells (Thome et al., 2014), and in cerebellar granule cells (Houston et al., 2017).

Occlusion did not affect the proportion of soma- vs. dendrite-origin AISs amongst the OB DA axon-bearing population (Soma: Ctrl n = 37, Occl n = 47; Dendrite: Ctrl n = 31, Occl n = 33; Fisher's exact test for proportions Ctrl vs Occl, p=0.62), nor did it affect the distance of the AIS start position from

656 the soma, independent of axon origin (Fig. 8C, note different symbols to indicate axon origin; Ctrl,
657 mean ± SEM 7.91 ± 0.73 μm, n = 68 cells, N = 4 mice; Occl, 8.47 ± 0.94 μm, n = 80 cells, N = 4 mice;
658 mixed model ANOVA of log-transformed AIS distance nested on mouse, effect of treatment
659 $F_{1,13} = 1.87$, $p = 0.19$; effect of axon origin, $F_{1,142} = 0.65$, $p = 0.42$; effect of interaction, $F_{1,142} = 1.94$,
660 $p = 0.17$). We did, however, find a sizeable and consistent activity-dependent difference in AIS
661 length, with AISs in occluded DA neurons being significantly shorter than those in control cells (Fig.
662 8D; Ctrl, mean ± SEM 20.74 ± 0.84 μm, n = 68 cells, N = 4 mice; Occluded 12.29 ± 0.66 μm, n = 80
663 cells, N = 4 mice; mixed model ANOVA nested on mouse, effect of treatment $F_{1,24} = 93$, $p < 0.0001$;
664 effect of axon origin $F_{1,145} = 0.74$, $p = 0.39$; effect of interaction, $F_{1,145} = 0.49$, $p = 0.49$). In a subset of
665 AnkG-labelled tissue where inter-slice variability was minimized with histological co-embedding (Fig.
666 6G), AIS shortening in response to brief sensory deprivation was not accompanied by any significant
667 change in the relative intensity of AnkG staining (Ctrl mean ± SEM 0.75 ± 0.048, n = 11; Occl
668 0.88 ± 0.055, n = 12; $t_{21} = 1.74$, $p = 0.10$), nor were AIS length and relative AnkG staining intensity
669 significantly correlated (Pearson $r = 0.21$, $n = 16$, $p = 0.44$). We also found no significant correlation
670 between AIS length and relative TH intensity (Pearson $r = -0.21$, $n = 16$, $p = 0.44$) suggesting that the
671 signaling pathways and cellular mechanisms underlying these two pathways in axon-bearing OB DA
672 cells may be reasonably independent (Chand et al., 2015; Cigola et al., 1998).
673
674 One key function of the AIS, which houses voltage-activated sodium channels at high density, is to
675 initiate action potentials (Kole et al., 2007). Previous experimental evidence (*e.g.,* (Evans et al., 2015;
676 Kuba et al., 2010)) and computational models (see, *e.g.*, (Goethals and Brette, 2020; Gulledge and
677 Bravo, 2016; Hamada et al., 2016)) have shown that alterations in AIS length, all else being equal, are
678 associated with decreases in neuronal excitability. So does the experience-dependent decrease in
679 AIS length we observe in axon-bearing DA cells correlate with a reduced ability to fire action
680 potentials? To test this prediction, we again turned to whole-cell patch clamp recordings in DAT-
681 tdTomato mice, but this time we targeted red cells with a large soma (Fig. 8E), and used the biphasic

682 nature of their action potential phase plots as a proxy for the presence of an AIS (see Materials and
683 Methods; Bean, 2007; Chand et al., 2015; Galliano et al., 2018). We found that, with no difference in
684 key passive properties such as resting membrane potential and membrane resistance (Table 5),
685 putative axon-bearing/biphasic DA cells recorded in acute slices obtained from occluded mice
686 needed more current to reach threshold to generate an action potential (Fig. 8G; Ctrl mean ± SEM
687 102 ± 11 pA, n = 9 cells; Occl, 148 ± 16 pA, n = 10 cells; unpaired t-test, $t_{17} = 2.30$, $p = 0.035$), and
688 they did so at a more depolarized membrane voltage (Fig. 8H; Ctrl mean ± SEM -32.58 ± 0.99, n = 9
689 cells; Occl -28.57 ± 0.78, n = 10 cells; unpaired t-test, $t_{17} = 3.23$, $p = 0.005$). Moreover, when
690 challenged with 500 ms-long current injections of increasing amplitude, occluded DA cells fired
691 fewer action potentials overall than control DA cells (Fig. 8I; mixed model ANOVA, effect of
692 treatment, $F_{1,31} = 6.89$, $p = 0.013$).
693
694 In summary, among the OB cell types we analysed, axon-bearing DA interneurons are the only group
695 that respond to brief, naturally-relevant sensory deprivation with a combination of biochemical (Fig.
696 6G), morphological (Fig. 8D) and intrinsic functional (Fig. 8G-I) plastic changes.
697

DISCUSSION

Our results demonstrate that, in young adult mice, brief 24 h sensory deprivation via the unilateral insertion of a custom-made naris plug is minimally-invasive yet sufficient to downregulate activity in olfactory bulb circuits. In response to this naturally-relevant manipulation (Fokkens et al., 2012) we find that a very specific subtype of local inhibitory interneurons – axon-bearing DA cells located in the glomerular layer – respond with activity-dependent structural plasticity at their AIS and co-incident changes in their intrinsic excitability.

Can we use structure to predict function *in vivo*? AIS properties and neuronal excitability

Whether on a canonical soma-origin axon or one that emanates from a dendrite, the AIS's structural properties (distance from soma and length) can have a major impact on a neuron's excitability. For the property of AIS position the precise nature of this impact remains unresolved, and is likely to depend on various factors including variation in neuronal morphology (Goethals and Brette, 2020; Gulledge and Bravo, 2016; Hamada et al., 2016; Parekh and Ascoli, 2015; Verbist et al., 2020). In contrast, changes in AIS length have a much clearer corollary. Experimental and theoretical results are in close agreement that, all else being equal, a shorter AIS leads to decreased excitability (Evans et al., 2015; Goethals and Brette, 2020; Grubb and Burrone, 2010; Gulledge and Bravo, 2016; Höfflin et al., 2017; Jamann et al., 2020; Kuba et al., 2010; Pan-Vazquez et al., 2020; Sohn et al., 2019; Wefelmeyer et al., 2015; Werginz et al., 2020). Our data showing brief sensory deprivation-induced AIS shortening and decreased excitability in OB DA neurons are entirely consistent with this coherent picture.

Importantly, while activity-dependent changes in both AIS position and length have been described in cultured neurons (Booker et al., 2020; Chand et al., 2015; Dumitrescu et al., 2016; Evans et al., 2013, 2015; Grubb and Burrone, 2010; Horschitz et al., 2015; Lezmy et al., 2017; Muir and Kittler, 2014; Sohn et al., 2019; Wefelmeyer et al., 2015), plasticity of AIS position without any

accompanying length change has yet to be described in intact networks. Indeed, to date all activity-dependent AIS plasticity described *in vivo* or in *ex vivo* acute slices seems to express itself as length changes (Fig. 8 here; (Del Pino et al., 2020; Höfflin et al., 2017; Jamann et al., 2020; Kuba et al., 2010; Pan-Vazquez et al., 2020)). Failure to describe *in vivo* AIS position changes could be due to a physical impediment to moving this macromolecular structure, which is tightly linked to extracellular matrix proteins (Brückner et al., 2006), when the overall 3D circuit structure is in place. Alternatively, *in vivo* AIS positional changes might be possible, but we have yet to probe the cell types that are capable of this with an appropriate manipulation. Finally, it is important to note that the main caveat of most *in vitro* and all *in vivo* AIS plasticity studies is that analysis has been done at the population level, and links between AIS and excitability changes on a cell-by-cell level are few and far between. Future studies will need to address this by pairing electrophysiological recordings with tools for AIS live imaging (Dumitrescu et al., 2016).

Implications for olfactory processing

We find here that 24 h sensory deprivation leaves bulbar excitatory neurons' intrinsic excitability unchanged, but recruits structural and intrinsic plastic mechanisms in a specialised population of inhibitory interneurons, as well as producing downregulated TH levels in all DA neurons. What are the functional implications of these different neuronal responses? By releasing GABA and dopamine that can target release probability at OSN terminals, DA neurons act as gain controllers at the first synapse in olfaction (Borisovska et al., 2013; Hsia et al., 1999; Vaaga et al., 2017). Thanks to their rapid activity-dependent regulation of TH expression, both subtypes of DA cell might respond to decreased afferent input by producing and releasing less dopamine, thus decreasing feedback inhibition of OSN terminals. This could be a very effective mechanism to rapidly counterbalance the effects of sensory deprivation by increasing the gain of the first synapse in the olfactory system, potentially thereby heightening odour sensitivity. Indeed, our data represent the fastest known description of this extremely well-described phenomenon which – at least following longer-term

manipulations – appears responsible for balancing bulbar input-output functions in the face of sensory deprivation (Baker et al., 1993; Cho et al., 1996; Wilson and Sullivan, 1995).

The AIS shortening and decreased excitability in axon-bearing DA cells could further accentuate the deprivation-associated relief of inhibition in the glomerular layer. Decreases in TH levels and decreases in neuronal excitability appear broadly synergistic, and together should locally increase the gain of nose-to-brain transmission. However, dopamine has recently been shown to have complex post-synaptic effects on glomerular circuitry (Liu, 2020), by which any changes in OSN presynaptic inhibition driven by plasticity in local DA cells might be at least partially counteracted. Also, axon-bearing DA cells have widely arborized dendritic trees and a long-spanning axon (Banerjee et al., 2015; Galliano et al., 2018; Kiyokage et al., 2017), and are believed to contribute not only to local intraglomerular signaling and gain control, but also, by means of long-range lateral inhibition (Banerjee et al., 2015; Liu et al., 2013; Whitesell et al., 2013), to odour identification and discrimination (Linster and Cleland, 2009; Uchida et al., 2000; Urban, 2002; Zavitz et al., 2020). Decreasing their excitability might therefore be expected to produce olfactory discrimination deficits. How can we reconcile these two potentially opposing effects? One could speculate that when the network is deprived of sensory inputs, a first, fast-acting response dampening all (intra- and interglomerular) inhibition to increase overall sensitivity (Kuhlman et al., 2013) could be prioritized over maintaining fine discrimination. Then, if the sensory deprivation persists, a more nuanced solution might be implemented in which other neuron types adapt their excitability to reach a new stable network set point, whilst permitting interglomerular connections to reprise their more powerful long-range inhibitory function (Gainey and Feldman, 2017). In addition, the long-range interglomerular projections of glomerular layer DA neurons have also been proposed to underlie gain control modulation of OSN→M/TC signaling (Banerjee et al., 2015; Bundschuh et al., 2012), so targeted decreases in their excitability could be another mechanism for ensuring maximal impact of diminished OSN inputs, especially in the initial stages once the state of deprivation begins

to resolve. In this way, specific plastic changes in one cell type might shift the balance of information processing in sensory circuits to prioritize detection over discrimination when input activity is diminished.

Homeostasis in cells or circuits? Inhibitory neurons as first responders

While not preponderant in cortex, inhibitory neurons constitute the main population in the olfactory bulb (Shepherd, 2004). Heterogeneous in all brain areas, inhibitory neurons can be just as plastic as their excitatory counterparts, but can respond differently to the same sensory input (Gainey and Feldman, 2017). Understanding this differential excitatory/inhibitory plasticity and its time course could help unpack one of the most puzzling phenomena in neuroscience: how stability and plasticity coexist to ensure both homeostasis and learning (Fox and Stryker, 2017). Indeed, one could speculate that while the plasticity of excitatory neurons is mostly Hebbian and aimed at supporting the acquisition of new associations (Bekisz et al., 2010; Gao et al., 2017; Yiu et al., 2014), one of the main functions of activity-dependent plasticity in inhibitory neurons is to act as 'first responders'. In this scheme, plasticity in local inhibitory cells acts to compensate a short-lived change in sensory input and to maintain homeostasis – not at the single-cell level, but at the network level. If then the sensory perturbation persists and becomes the 'new normal', excitatory cells might need to activate homeostatic plasticity mechanisms and inhibitory neurons to downscale their own fast-acting plastic response, to reach a new network set point while maintaining an appropriate dynamic range (Gainey and Feldman, 2017; Keck et al., 2017; Turrigiano, 2012; Wefelmeyer et al., 2016). The overall circuit response to a changed sensory stimulus cannot thus be inferred by solely looking at principal neurons (Hennequin et al., 2017), or by simple arithmetic sums of plastic changes in the various neuron types, or without appreciation of the length and scope of sensory manipulation. Future studies will need to holistically address how activity-dependent plasticity is differentially expressed in inhibitory and excitatory neurons in order to shape information processing in distinct brain circuits.

802

803 **REFERENCES**

804 Aarts, E., Verhage, M., Veenvliet, J.V., Dolan, C.V., and van der Sluis, S. (2014). A solution to
805 dependency: using multilevel analysis to accommodate nested data. Nat. Neurosci. *17*, 491–496.

806 Akiba, Y., Sasaki, H., Saino-Saito, S., and Baker, H. (2007). Temporal and spatial disparity in cFOS
807 expression and dopamine phenotypic differentiation in the neonatal mouse olfactory bulb.
808 Neurochem. Res. *32*, 625–634.

809 Akter, N., Fukaya, R., Adachi, R., Kawabe, H., and Kuba, H. (2020). Structural and Functional
810 Refinement of the Axon Initial Segment in Avian Cochlear Nucleus during Development. J. Neurosci.
811 Off. J. Soc. Neurosci. *40*, 6709–6721.

812 Ashwell, K.W.S. (2006). Chemoarchitecture of the monotreme olfactory bulb. Brain. Behav. Evol. *67*,
813 69–84.

814 Bäckman, C.M., Malik, N., Zhang, Y., Shan, L., Grinberg, A., Hoffer, B.J., Westphal, H., and Tomac, A.C.
815 (2006). Characterization of a mouse strain expressing Cre recombinase from the 3' untranslated
816 region of the dopamine transporter locus. Genes. N. Y. N 2000 *44*, 383–390.

817 Baker, H., Morel, K., Stone, D.M., and Maruniak, J.A. (1993). Adult naris closure profoundly reduces
818 tyrosine hydroxylase expression in mouse olfactory bulb. Brain Res. *614*, 109–116.

819 Banerjee, A., Marbach, F., Anselmi, F., Koh, M.S., Davis, M.B., Garcia da Silva, P., Delevich, K., Oyibo,
820 H.K., Gupta, P., Li, B., et al. (2015). An Interglomerular Circuit Gates Glomerular Output and
821 Implements Gain Control in the Mouse Olfactory Bulb. Neuron *87*, 193–207.

822 Baranauskas, G., Mukovskiy, A., Wolf, F., and Volgushev, M. (2010). The determinants of the onset
823 dynamics of action potentials in a computational model. Neuroscience *167*, 1070–1090.

824 Barnes, S.J., Sammons, R.P., Jacobsen, R.I., Mackie, J., Keller, G.B., and Keck, T. (2015). Subnetwork-
825 Specific Homeostatic Plasticity in Mouse Visual Cortex In Vivo. Neuron *86*, 1290–1303.

826 Bean, B.P. (2007). The action potential in mammalian central neurons. Nat. Rev. Neurosci. *8*, 451–
827 465.

828 Bekisz, M., Garkun, Y., Wabno, J., Hess, G., Wrobel, A., and Kossut, M. (2010). Increased excitability of
829 cortical neurons induced by associative learning: an ex vivo study: Learning-induced increase of
830 cortical neuronal excitability. Eur. J. Neurosci. *32*, 1715–1725.

831 Bender, K.J., and Trussell, L.O. (2012). The physiology of the axon initial segment. Annu. Rev.
832 Neurosci. *35*, 249–265.

833 Bojsen-Moller, F., and Fahrenkrug, J. (1971). Nasal swell-bodies and cyclic changes in the air passage
834 of the rat and rabbit nose. J. Anat. *110*, 25–37.

835 Bonzano, S., Bovetti, S., Gendusa, C., Peretto, P., and De Marchis, S. (2016). Adult Born Olfactory Bulb
836 Dopaminergic Interneurons: Molecular Determinants and Experience-Dependent Plasticity. Front.
837 Neurosci. *10*, 189.

838 Booker, S.A., Simões de Oliveira, L., Anstey, N.J., Kozic, Z., Dando, O.R., Jackson, A.D., Baxter, P.S.,
839 Isom, L.L., Sherman, D.L., Hardingham, G.E., et al. (2020). Input-Output Relationship of CA1
840 Pyramidal Neurons Reveals Intact Homeostatic Mechanisms in a Mouse Model of Fragile X
841 Syndrome. Cell Rep. *32*, 107988.

842 Borisovska, M., Bensen, A.L., Chong, G., and Westbrook, G.L. (2013). Distinct modes of dopamine and
843 GABA release in a dual transmitter neuron. J. Neurosci. Off. J. Soc. Neurosci. *33*, 1790–1796.

844 Brückner, G., Szeöke, S., Pavlica, S., Grosche, J., and Kacza, J. (2006). Axon initial segment ensheathed
845 by extracellular matrix in perineuronal nets. Neuroscience *138*, 365–375.

Brzosko, Z., Mierau, S.B., and Paulsen, O. (2019). Neuromodulation of Spike-Timing-Dependent Plasticity: Past, Present, and Future. Neuron *103*, 563–581.

Bundschuh, S.T., Zhu, P., Schärer, Y.-P.Z., and Friedrich, R.W. (2012). Dopaminergic modulation of mitral cells and odor responses in the zebrafish olfactory bulb. J. Neurosci. Off. J. Soc. Neurosci. *32*, 6830–6840.

Byrne, D.J., Lipovsek, M., and Grubb, M.S. (2020). Brief sensory deprivation triggers plasticity of neurotransmitter-synthesising enzyme expression in genetically labelled olfactory bulb dopaminergic neurons. BioRxiv 2020.06.03.132555.

Chand, A.N., Galliano, E., Chesters, R.A., and Grubb, M.S. (2015). A distinct subtype of dopaminergic interneuron displays inverted structural plasticity at the axon initial segment. J. Neurosci. Off. J. Soc. Neurosci. *35*, 1573–1590.

Cheetham, C.E.J., Park, U., and Belluscio, L. (2016). Rapid and continuous activity-dependent plasticity of olfactory sensory input. Nat. Commun. *7*, 1–11.

Cho, J.Y., Min, N., Franzen, L., and Baker, H. (1996). Rapid down-regulation of tyrosine hydroxylase expression in the olfactory bulb of naris-occluded adult rats. J. Comp. Neurol. *369*, 264–276.

Cigola, E., Volpe, B.T., Lee, J.W., Franzen, L., and Baker, H. (1998). Tyrosine hydroxylase expression in primary cultures of olfactory bulb: role of L-type calcium channels. J. Neurosci. Off. J. Soc. Neurosci. *18*, 7638–7649.

Citri, A., and Malenka, R.C. (2008). Synaptic plasticity: multiple forms, functions, and mechanisms. Neuropsychopharmacol. Off. Publ. Am. Coll. Neuropsychopharmacol. *33*, 18–41.

Cockerham, R.E., Margolis, F.L., and Munger, S.D. (2009). Afferent activity to necklace glomeruli is dependent on external stimuli. BMC Res. Notes *2*, 31.

Coombs, J.S., Curtis, D.R., and Eccles, J.C. (1957). The generation of impulses in motoneurones. J. Physiol. *139*, 232–249.

Coppola, D.M. (2012). Studies of olfactory system neural plasticity: the contribution of the unilateral naris occlusion technique. Neural Plast. *2012*, 351752.

Cummings, D.M., and Belluscio, L. (2010). Continuous neural plasticity in the olfactory intrabulbar circuitry. J. Neurosci. Off. J. Soc. Neurosci. *30*, 9172–9180.

Cummings, D.M., and Brunjes, P.C. (1997). The Effects of Variable Periods of Functional Deprivation on Olfactory Bulb Development in Rats. Exp. Neurol. *148*, 360–366.

Cummings, D.M., Snyder, J.S., Brewer, M., Cameron, H.A., and Belluscio, L. (2014). Adult neurogenesis is necessary to refine and maintain circuit specificity. J. Neurosci. Off. J. Soc. Neurosci. *34*, 13801–13810.

De Marchis, S., Bovetti, S., Carletti, B., Hsieh, Y.-C., Garzotto, D., Peretto, P., Fasolo, A., Puche, A.C., and Rossi, F. (2007). Generation of Distinct Types of Periglomerular Olfactory Bulb Interneurons during Development and in Adult Mice: Implication for Intrinsic Properties of the Subventricular Zone Progenitor Population. J. Neurosci. *27*, 657–664.

Debanne, D., Inglebert, Y., and Russier, M. (2019). Plasticity of intrinsic neuronal excitability. Curr. Opin. Neurobiol. *54*, 73–82.

Del Pino, I., Tocco, C., Magrinelli, E., Marcantoni, A., Ferraguto, C., Tomagra, G., Bertacchi, M., Alfano, C., Leinekugel, X., Frick, A., et al. (2020). COUP-TFI/Nr2f1 Orchestrates Intrinsic Neuronal Activity during Development of the Somatosensory Cortex. Cereb. Cortex *30*, 5667–5685.

Ding, Y., Chen, T., Wang, Q., Yuan, Y., and Hua, T. (2018). Axon initial segment plasticity accompanies enhanced excitation of visual cortical neurons in aged rats. Neuroreport *29*, 1537–1543.

Dumitrescu, A.S., Evans, M.D., and Grubb, M.S. (2016). Evaluating Tools for Live Imaging of Structural Plasticity at the Axon Initial Segment. Front. Cell. Neurosci. *10*.

Evans, M.D., Sammons, R.P., Lebron, S., Dumitrescu, A.S., Watkins, T.B.K., Uebele, V.N., Renger, J.J., and Grubb, M.S. (2013). Calcineurin Signaling Mediates Activity-Dependent Relocation of the Axon Initial Segment. J. Neurosci. *33*, 6950–6963.

Evans, M.D., Dumitrescu, A.S., Kruijssen, D.L.H., Taylor, S.E., and Grubb, M.S. (2015). Rapid Modulation of Axon Initial Segment Length Influences Repetitive Spike Firing. Cell Rep. *13*, 1233–1245.

Fokkens, W.J., Bachert, C., Douglas, R., Gevaert, P., Georgalas, C., Harvey, R., Hellings, P., Hopkins, C., Jones, N., Joos, G., et al. (2012). European Position Paper on Rhinosinusitis and Nasal Polyps 2012. Rhinology *50*, 329.

Foust, A., Popovic, M., Zecevic, D., and McCormick, D.A. (2010). Action potentials initiate in the axon initial segment and propagate through axon collaterals reliably in cerebellar Purkinje neurons. J. Neurosci. Off. J. Soc. Neurosci. *30*, 6891–6902.

Fox, K., and Stryker, M. (2017). Integrating Hebbian and homeostatic plasticity: introduction. Philos. Trans. R. Soc. Lond. B. Biol. Sci. *372*.

Gainey, M.A., and Feldman, D.E. (2017). Multiple shared mechanisms for homeostatic plasticity in rodent somatosensory and visual cortex. Philos. Trans. R. Soc. Lond. B. Biol. Sci. *372*.

Galliano, E., Franzoni, E., Breton, M., Chand, A.N., Byrne, D.J., Murthy, V.N., and Grubb, M.S. (2018). Embryonic and postnatal neurogenesis produce functionally distinct subclasses of dopaminergic neuron. ELife *7*.

Gao, Y., Budlong, C., Durlacher, E., and Davison, I.G. (2017). Neural mechanisms of social learning in

the female mouse. ELife *6*, e25421.

Gire, D.H., Franks, K.M., Zak, J.D., Tanaka, K.F., Whitesell, J.D., Mulligan, A.A., Hen, R., and Schoppa, N.E. (2012). Mitral Cells in the Olfactory Bulb Are Mainly Excited through a Multistep Signaling Path. J. Neurosci. *32*, 2964–2975.

Goethals, S., and Brette, R. (2020). Theoretical relation between axon initial segment geometry and excitability. ELife *9*.

González-Cabrera, C., Meza, R., Ulloa, L., Merino-Sepúlveda, P., Luco, V., Sanhueza, A., Oñate-Ponce, A., Bolam, J.P., and Henny, P. (2017). Characterization of the axon initial segment of mice substantia nigra dopaminergic neurons. J. Comp. Neurol. *525*, 3529–3542.

Grier, B.D., Belluscio, L., and Cheetham, C.E.J. (2016). Olfactory Sensory Activity Modulates Microglial-Neuronal Interactions during Dopaminergic Cell Loss in the Olfactory Bulb. Front. Cell. Neurosci. *10*.

Grubb, M.S., and Burrone, J. (2010). Activity-dependent relocation of the axon initial segment fine-tunes neuronal excitability. Nature *465*, 1070–1074.

Gulledge, A.T., and Bravo, J.J. (2016). Neuron Morphology Influences Axon Initial Segment Plasticity. ENeuro *3*.

Gutzmann, A., Ergül, N., Grossmann, R., Schultz, C., Wahle, P., and Engelhardt, M. (2014). A period of structural plasticity at the axon initial segment in developing visual cortex. Front. Neuroanat. *8*, 11.

Hamada, M.S., Goethals, S., de Vries, S.I., Brette, R., and Kole, M.H.P. (2016). Covariation of axon initial segment location and dendritic tree normalizes the somatic action potential. Proc. Natl. Acad. Sci. U. S. A. *113*, 14841–14846.

Hamdan, H., Lim, B.C., Torii, T., Joshi, A., Konning, M., Smith, C., Palmer, D.J., Ng, P., Leterrier, C.,

934 Oses-Prieto, J.A., et al. (2020). Mapping axon initial segment structure and function by multiplexed
935 proximity biotinylation. Nat. Commun. *11*, 1–17.

936 Hartmann, K., Bruehl, C., Golovko, T., and Draguhn, A. (2008). Fast Homeostatic Plasticity of Inhibition
937 via Activity-Dependent Vesicular Filling. PLOS ONE *3*, e2979.

938 Hedstrom, K.L., Ogawa, Y., and Rasband, M.N. (2008). AnkyrinG is required for maintenance of the
939 axon initial segment and neuronal polarity. J. Cell Biol. *183*, 635–640.

940 Hennequin, G., Agnes, E.J., and Vogels, T.P. (2017). Inhibitory Plasticity: Balance, Control, and
941 Codependence. Annu. Rev. Neurosci. *40*, 557–579.

942 Henny, P., Brown, M.T.C., Northrop, A., Faunes, M., Ungless, M.A., Magill, P.J., and Bolam, J.P. (2012).
943 Structural correlates of heterogeneous in vivo activity of midbrain dopaminergic neurons. Nat.
944 Neurosci. *15*, 613–619.

945 Höfflin, F., Jack, A., Riedel, C., Mack-Bucher, J., Roos, J., Corcelli, C., Schultz, C., Wahle, P., and
946 Engelhardt, M. (2017). Heterogeneity of the Axon Initial Segment in Interneurons and Pyramidal Cells
947 of Rodent Visual Cortex. Front. Cell. Neurosci. *11*, 332.

948 Horschitz, S., Matthäus, F., Groß, A., Rosner, J., Galach, M., Greffrath, W., Treede, R.-D., Utikal, J.,
949 Schloss, P., and Meyer-Lindenberg, A. (2015). Impact of preconditioning with retinoic acid during
950 early development on morphological and functional characteristics of human induced pluripotent
951 stem cell-derived neurons. Stem Cell Res 30–41.

952 Houston, C.M., Diamanti, E., Diamantaki, M., Kutsarova, E., Cook, A., Sultan, F., and Brickley, S.G.
953 (2017). Exploring the significance of morphological diversity for cerebellar granule cell excitability.
954 Sci. Rep. *7*, 46147.

955 Hsia, A.Y., Vincent, J.D., and Lledo, P.M. (1999). Dopamine depresses synaptic inputs into the

olfactory bulb. J. Neurophysiol. *82*, 1082–1085.

Imai, T. (2014). Construction of functional neuronal circuitry in the olfactory bulb. Semin. Cell Dev. Biol. *35*, 180–188.

Jamann, N., Dannehl, D., Wagener, R., Corcelli, C., Schultz, C., Staiger, J., Kole, M.H.P., and Engelhardt, M. (2020). Sensory input drives rapid homeostatic scaling of the axon initial segment in mouse barrel cortex. BioRxiv 2020.02.27.968065.

Jenerick, H. (1963). Phase Plane Trajectories of the Muscle Spike Potential. Biophys. J. *3*, 363–377.

Kahana-Zweig, R., Geva-Sagiv, M., Weissbrod, A., Secundo, L., Soroker, N., and Sobel, N. (2016). Measuring and Characterizing the Human Nasal Cycle. PloS One *11*, e0162918.

Kaifosh, P., and Losonczy, A. (2014). The Inside Track: Privileged Neural Communication through Axon-Carrying Dendrites. Neuron *83*, 1231–1234.

Kass, M.D., Pottackal, J., Turkel, D.J., and McGann, J.P. (2013). Changes in the neural representation of odorants after olfactory deprivation in the adult mouse olfactory bulb. Chem. Senses *38*, 77–89.

Keck, T., Toyoizumi, T., Chen, L., Doiron, B., Feldman, D.E., Fox, K., Gerstner, W., Haydon, P.G., Hübener, M., Lee, H.-K., et al. (2017). Integrating Hebbian and homeostatic plasticity: the current state of the field and future research directions. Philos. Trans. R. Soc. Lond. B. Biol. Sci. *372*.

Khaliq, Z.M., Gouwens, N.W., and Raman, I.M. (2003). The contribution of resurgent sodium current to high-frequency firing in Purkinje neurons: an experimental and modeling study. J. Neurosci. Off. J. Soc. Neurosci. *23*, 4899–4912.

Kikuta, S., Sakamoto, T., Nagayama, S., Kanaya, K., Kinoshita, M., Kondo, K., Tsunoda, K., Mori, K., and Yamasoba, T. (2015). Sensory deprivation disrupts homeostatic regeneration of newly generated olfactory sensory neurons after injury in adult mice. J. Neurosci. Off. J. Soc. Neurosci. *35*, 2657–2673.

978 Kiyokage, E., Kobayashi, K., and Toida, K. (2017). Spatial distribution of synapses on tyrosine
979 hydroxylase-expressing juxtaglomerular cells in the mouse olfactory glomerulus. J. Comp. Neurol.
980 *525*, 1059–1074.

981 Knight, Z.A., Tan, K., Birsoy, K., Schmidt, S., Garrison, J.L., Wysocki, R.W., Emiliano, A., Ekstrand, M.I.,
982 and Friedman, J.M. (2012). Molecular Profiling of Activated Neurons by Phosphorylated Ribosome
983 Capture. Cell *151*.

984 Knott, G.W., Quairiaux, C., Genoud, C., and Welker, E. (2002). Formation of dendritic spines with
985 GABAergic synapses induced by whisker stimulation in adult mice. Neuron *34*, 265–273.

986 Kole, M.H.P., Letzkus, J.J., and Stuart, G.J. (2007). Axon Initial Segment Kv1 Channels Control Axonal
987 Action Potential Waveform and Synaptic Efficacy. Neuron *55*, 633–647.

988 Korshunov, K.S., Blakemore, L.J., Bertram, R., and Trombley, P.Q. (2020). Spiking and Membrane
989 Properties of Rat Olfactory Bulb Dopamine Neurons. Front. Cell. Neurosci. *14*, 60.

990 Kosaka, T., Katsumaru, H., Hama, K., Wu, J.Y., and Heizmann, C.W. (1987). GABAergic neurons
991 containing the Ca2+-binding protein parvalbumin in the rat hippocampus and dentate gyrus. Brain
992 Res. *419*, 119–130.

993 Kosaka, T., Komada, M., and Kosaka, K. (2008). Sodium channel cluster, betaIV-spectrin and ankyrinG
994 positive “hot spots” on dendritic segments of parvalbumin-containing neurons and some other
995 neurons in the mouse and rat main olfactory bulbs. Neurosci. Res. *62*, 176–186.

996 Kosaka, T., Pignatelli, A., and Kosaka, K. (2019). Heterogeneity of tyrosine hydroxylase expressing
997 neurons in the main olfactory bulb of the mouse. Neurosci. Res.

998 Kuba, H., Oichi, Y., and Ohmori, H. (2010). Presynaptic activity regulates Na(+) channel distribution at
999 the axon initial segment. Nature *465*, 1075–1078.

1000 Kuba, H., Yamada, R., Ishiguro, G., and Adachi, R. (2015). Redistribution of Kv1 and Kv7 enhances
1001 neuronal excitability during structural axon initial segment plasticity. Nat. Commun. *6*, 1–12.

1002 Kuhlman, S.J., Olivas, N.D., Tring, E., Ikrar, T., Xu, X., and Trachtenberg, J.T. (2013). A disinhibitory
1003 microcircuit initiates critical-period plasticity in the visual cortex. Nature *501*, 543–546.

1004 Kullmann, D.M., Moreau, A.W., Bakiri, Y., and Nicholson, E. (2012). Plasticity of inhibition. Neuron *75*,
1005 951–962.

1006 Leterrier, C. (2018). The Axon Initial Segment: An Updated Viewpoint. J. Neurosci. Off. J. Soc.
1007 Neurosci. *38*, 2135–2145.

1008 Lezmy, J., Lipinsky, M., Khrapunsky, Y., Patrich, E., Shalom, L., Peretz, A., Fleidervish, I.A., and Attali, B.
1009 (2017). M-current inhibition rapidly induces a unique CK2-dependent plasticity of the axon initial
1010 segment. Proc. Natl. Acad. Sci. *114*, E10234–E10243.

1011 Linster, C., and Cleland, T.A. (2009). Glomerular microcircuits in the olfactory bulb. Neural Netw. Off.
1012 J. Int. Neural Netw. Soc. *22*, 1169–1173.

1013 Liu, S. (2020). Dopaminergic Modulation of Glomerular Circuits in the Mouse Olfactory Bulb. Front.
1014 Cell. Neurosci. *14*, 172.

1015 Liu, S., and Shipley, M.T. (2008). Multiple conductances cooperatively regulate spontaneous bursting
1016 in mouse olfactory bulb external tufted cells. J. Neurosci. Off. J. Soc. Neurosci. *28*, 1625–1639.

1017 Liu, W.L., and Shipley, M.T. (1994). Intrabulbar associational system in the rat olfactory bulb
1018 comprises cholecystokinin-containing tufted cells that synapse onto the dendrites of GABAergic
1019 granule cells. J. Comp. Neurol. *346*, 541–558.

1020 Liu, S., Plachez, C., Shao, Z., Puche, A., and Shipley, M.T. (2013). Olfactory bulb short axon cell release
1021 of GABA and dopamine produces a temporally biphasic inhibition-excitation response in external

1022 tufted cells. J. Neurosci. Off. J. Soc. Neurosci. *33*, 2916–2926.

1023 Lledo, P.-M., Alonso, M., and Grubb, M.S. (2006). Adult neurogenesis and functional plasticity in
1024 neuronal circuits. Nat. Rev. Neurosci. *7*, 179–193.

1025 Lodovichi, C., Belluscio, L., and Katz, L.C. (2003). Functional topography of connections linking mirror-
1026 symmetric maps in the mouse olfactory bulb. Neuron *38*, 265–276.

1027 Madisen, L., Zwingman, T.A., Sunkin, S.M., Oh, S.W., Zariwala, H.A., Gu, H., Ng, L.L., Palmiter, R.D.,
1028 Hawrylycz, M.J., Jones, A.R., et al. (2010). A robust and high-throughput Cre reporting and
1029 characterization system for the whole mouse brain. Nat. Neurosci. *13*, 133–140.

1030 McGann, J.P. (2013). Presynaptic Inhibition of Olfactory Sensory Neurons: New Mechanisms and
1031 Potential Functions. Chem. Senses *38*, 459–474.

1032 Meyer, G., and Wahle, P. (1988). Early postnatal development of cholecystokinin-immunoreactive
1033 structures in the visual cortex of the cat. J. Comp. Neurol. *276*, 360–386.

1034 Meza, R.C., López-Jury, L., Canavier, C.C., and Henny, P. (2018). Role of the Axon Initial Segment in the
1035 Control of Spontaneous Frequency of Nigral Dopaminergic NeuronsIn Vivo. J. Neurosci. Off. J. Soc.
1036 Neurosci. *38*, 733–744.

1037 Morales, M., and Margolis, E.B. (2017). Ventral tegmental area: cellular heterogeneity, connectivity
1038 and behaviour. Nat. Rev. Neurosci. *18*, 73–85.

1039 Moubarak, E., Engel, D., Dufour, M.A., Tapia, M., Tell, F., and Goaillard, J.-M. (2019). Robustness to
1040 Axon Initial Segment Variation Is Explained by Somatodendritic Excitability in Rat Substantia Nigra
1041 Dopaminergic Neurons. J. Neurosci. Off. J. Soc. Neurosci. *39*, 5044–5063.

1042 Muir, J., and Kittler, J.T. (2014). Plasticity of GABAA receptor diffusion dynamics at the axon initial
1043 segment. Front. Cell. Neurosci. *8*.

1044 Nadi, N.S., Head, R., Grillo, M., Hempstead, J., Grannot-Reisfeld, N., and Margolis, F.L. (1981).
1045 Chemical deafferentation of the olfactory bulb: plasticity of the levels of tyrosine hydroxylase,
1046 dopamine and norepinephrine. Brain Res. *213*, 365–377.

1047 Najac, M., De Saint Jan, D., Reguero, L., Grandes, P., and Charpak, S. (2011). Monosynaptic and
1048 polysynaptic feed-forward inputs to mitral cells from olfactory sensory neurons. J. Neurosci. Off. J.
1049 Soc. Neurosci. *31*, 8722–8729.

1050 Pan-Vazquez, A., Wefelmeyer, W., Gonzalez Sabater, V., Neves, G., and Burrone, J. (2020). Activity-
1051 Dependent Plasticity of Axo-axonic Synapses at the Axon Initial Segment. Neuron.

1052 Parekh, R., and Ascoli, G.A. (2015). Quantitative investigations of axonal and dendritic arbors:
1053 development, structure, function, and pathology. Neurosci. Rev. J. Bringing Neurobiol. Neurol.
1054 Psychiatry *21*, 241–254.

1055 Pignatelli, A., Kobayashi, K., Okano, H., and Belluzzi, O. (2005). Functional properties of dopaminergic
1056 neurones in the mouse olfactory bulb. J. Physiol. *564*, 501–514.

1057 Romanov, R.A., Zeisel, A., Bakker, J., Girach, F., Hellysaz, A., Tomer, R., Alpár, A., Mulder, J., Clotman,
1058 F., Keimpema, E., et al. (2017). Molecular interrogation of hypothalamic organization reveals distinct
1059 dopamine neuronal subtypes. Nat. Neurosci. *20*, 176–188.

1060 Roy, A., Osik, J.J., Meschede-Krasa, B., Alford, W.T., Leman, D.P., and Van Hooser, S.D. (2020). Synaptic
1061 and intrinsic mechanisms underlying development of cortical direction selectivity. ELife *9*, e58509.

1062 Sanz Diez, A., Najac, M., and De Saint Jan, D. (2019). Basal forebrain GABAergic innervation of
1063 olfactory bulb periglomerular interneurons. J. Physiol. *597*, 2547–2563.

1064 Shepherd, G.M. (2004). The synaptic organization of the brain, 5th ed (New York, NY, US: Oxford
1065 University Press).

1066 Shepherd, G.M. (2005). Outline of a theory of olfactory processing and its relevance to humans.
1067 Chem. Senses *30 Suppl 1*, i3-5.

1068 Shu, Y., Duque, A., Yu, Y., Haider, B., and McCormick, D.A. (2007). Properties of Action-Potential
1069 Initiation in Neocortical Pyramidal Cells: Evidence From Whole Cell Axon Recordings. J. Neurophysiol.
1070 *97*, 746–760.

1071 Sohn, P.D., Huang, C.T.-L., Yan, R., Fan, L., Tracy, T.E., Camargo, C.M., Montgomery, K.M., Arhar, T.,
1072 Mok, S.-A., Freilich, R., et al. (2019). Pathogenic Tau Impairs Axon Initial Segment Plasticity and
1073 Excitability Homeostasis. Neuron *104*, 458-470.e5.

1074 Thome, C., Kelly, T., Yanez, A., Schultz, C., Engelhardt, M., Cambridge, S.B., Both, M., Draguhn, A.,
1075 Beck, H., and Egorov, A.V. (2014). Axon-carrying dendrites convey privileged synaptic input in
1076 hippocampal neurons. Neuron *83*, 1418–1430.

1077 Triarhou, L.C. (2014). Axons emanating from dendrites: phylogenetic repercussions with Cajalian
1078 hues. Front. Neuroanat. *8*.

1079 Turrigiano, G. (2012). Homeostatic Synaptic Plasticity: Local and Global Mechanisms for Stabilizing
1080 Neuronal Function. Cold Spring Harb. Perspect. Biol. *4*, a005736.

1081 Uchida, N., Takahashi, Y.K., Tanifuji, M., and Mori, K. (2000). Odor maps in the mammalian olfactory
1082 bulb: domain organization and odorant structural features. Nat. Neurosci. *3*, 1035–1043.

1083 Urban, N.N. (2002). Lateral inhibition in the olfactory bulb and in olfaction. Physiol. Behav. *77*, 607–
1084 612.

1085 Vaaga, C.E., Yorgason, J.T., Williams, J.T., and Westbrook, G.L. (2017). Presynaptic gain control by
1086 endogenous cotransmission of dopamine and GABA in the olfactory bulb. J. Neurophysiol. *117*,
1087 1163–1170.

1088 Vassilopoulos, S., Gibaud, S., Jimenez, A., Caillol, G., and Leterrier, C. (2019). Ultrastructure of the
1089 axonal periodic scaffold reveals a braid-like organization of actin rings. Nat. Commun. *10*, 5803.

1090 Verbist, C., Müller, M.G., Mansvelder, H.D., Legenstein, R., and Giugliano, M. (2020). The location of
1091 the axon initial segment affects the bandwidth of spike initiation dynamics. PLoS Comput. Biol. *16*,
1092 e1008087.

1093 Vlug, A.S., Teuling, E., Haasdijk, E.D., French, P., Hoogenraad, C.C., and Jaarsma, D. (2005). ATF3
1094 expression precedes death of spinal motoneurons in amyotrophic lateral sclerosis-SOD1 transgenic
1095 mice and correlates with c-Jun phosphorylation, CHOP expression, somato-dendritic ubiquitination
1096 and Golgi fragmentation. Eur. J. Neurosci. *22*, 1881–1894.

1097 Volgushev, M., Malyshev, A., Balaban, P., Chistiakova, M., Volgushev, S., and Wolf, F. (2008). Onset
1098 Dynamics of Action Potentials in Rat Neocortical Neurons and Identified Snail Neurons:
1099 Quantification of the Difference. PLoS ONE *3*, e1962.

1100 Wefelmeyer, W., Cattaert, D., and Burrone, J. (2015). Activity-dependent mismatch between axo-
1101 axonic synapses and the axon initial segment controls neuronal output. Proc. Natl. Acad. Sci. *112*,
1102 9757–9762.

1103 Wefelmeyer, W., Puhl, C.J., and Burrone, J. (2016). Homeostatic Plasticity of Subcellular Neuronal
1104 Structures: From Inputs to Outputs. Trends Neurosci. *39*, 656–667.

1105 Werginz, P., Raghuram, V., and Fried, S.I. (2020). Tailoring of the axon initial segment shapes the
1106 conversion of synaptic inputs into spiking output in OFF-α T retinal ganglion cells. Sci. Adv. *6*.

1107 Whitesell, J.D., Sorensen, K.A., Jarvie, B.C., Hentges, S.T., and Schoppa, N.E. (2013). Interglomerular
1108 lateral inhibition targeted on external tufted cells in the olfactory bulb. J. Neurosci. Off. J. Soc.
1109 Neurosci. *33*, 1552–1563.

1110 Wilson, D., and Sullivan, R. (1995). The D2 antagonist spiperone mimics the effects of olfactory
1111 deprivation on mitral/tufted cell odor response patterns. J. Neurosci. *15*, 5574–5581.

1112 Wu, R., Liu, Y., Wang, L., Li, B., and Xu, F. (2017). Activity Patterns Elicited by Airflow in the Olfactory
1113 Bulb and Their Possible Functions. J. Neurosci. *37*, 10700–10711.

1114 Yang, J., Xiao, Y., Li, L., He, Q., Li, M., and Shu, Y. (2019). Biophysical Properties of Somatic and Axonal
1115 Voltage-Gated Sodium Channels in Midbrain Dopaminergic Neurons. Front. Cell. Neurosci. *13*, 317.

1116 Yin, J., and Yuan, Q. (2014). Structural homeostasis in the nervous system: a balancing act for wiring
1117 plasticity and stability. Front. Cell. Neurosci. *8*, 439.

1118 Yiu, A.P., Mercaldo, V., Yan, C., Richards, B., Rashid, A.J., Hsiang, H.-L.L., Pressey, J., Mahadevan, V.,
1119 Tran, M.M., Kushner, S.A., et al. (2014). Neurons Are Recruited to a Memory Trace Based on Relative
1120 Neuronal Excitability Immediately before Training. Neuron *83*, 722–735.

1121 Zavitz, D., Youngstrom, I.A., Borisyuk, A., and Wachowiak, M. (2020). Effect of Interglomerular
1122 Inhibitory Networks on Olfactory Bulb Odor Representations. J. Neurosci. Off. J. Soc. Neurosci. *40*,
1123 5954–5969.

1124 Zhang, D.-Q., Zhou, T.-R., and McMahon, D.G. (2007). Functional Heterogeneity of Retinal
1125 Dopaminergic Neurons Underlying Their Multiple Roles in Vision. J. Neurosci. *27*, 692–699.

1126

1127

FIGURE LEGENDS

Figure 1. Brief unilateral naris occlusion does not damage the olfactory epithelium. (A) Left: schematic representation of the custom-made plug (orange) blocking air flow in the mouse nasal cavity without contacting the olfactory epithelium (OE). OB, olfactory bulb. Right: timeline of sensory manipulation. **(B)** Example images of olfactory epithelia in control and occluded mice. Arrow indicates rare Caspase-3-positive cells. **(C)** Thickness of the olfactory epithelium in control and occluded mice. **(D)** Density of OMP-positive cells in control and occluded mice. **(E)** Density of Caspase-3-positive cells in control and occluded mice. In **(C-E)**, empty circles represent individual sample regions; different colours indicate different mice; thick line shows mean ± SEM.

Figure 2. Brief unilateral naris occlusion decreases activity levels in both major subtypes of olfactory bulb dopaminergic neurons. (A) Schematic representation of the experimental design: coronal OB slices from one control and one occluded (X) mouse were co-embedded in an agarose block ("set") and processed and analysed together (see Materials and Methods). **(B)** Example maximum intensity projection image of dopaminergic (DA) neurons visualized via anti-tyrosine hydroxylase (TH) staining, and label for the activity early gene cFos, in control and occluded mice. Note that the brightness of the TH channel has been adjusted independently in these control and occluded example images (dimmed and enhanced, respectively) to make DA cell identity clear; the cFos channels have not been altered. onl, olfactory nerve layer; gl, glomerular layer; epl, external plexiform layer. Arrows indicate TH-positive/cFos-positive cells, arrowheads indicate TH-negative/cFos-positive cells. **(C)** Mean normalised cFos intensity in TH-positive cells of any soma size in control and occluded mice. **(D)** Normalized cFos intensity in TH-positive cells with soma area < 70 μm^2 (putative anaxonic DA cells), from 3 sets of control and occluded mice. **(E)** Normalized cFos intensity in TH-positive cells with soma size > 99 μm^2 (putative axon-bearing DA cells), from 3 sets of control and occluded mice. **(F)** Example images of cFos expression in TH-positive cells with an

identified ankyrin-G (AnkG)-positive AIS (arrows). The solid line indicates the emergence of the axonal process from the soma (asterisk). Note the different levels of cFos signal and background in the two example images, which were taken from the same co-embedded set but from different slices. **(G)** Normalized cFos intensity in AnkG-positive/TH-positive cells in control and occluded mice. In **(D,E,G)**, empty circles represent individual cells and different colours indicate different mice; thick lines show mean ± SEM; *, $p < 0.05$, ***= $p < 0.0001$.

Figure 3. Brief unilateral naris occlusion decreases activity levels in bulbar excitatory neurons. (A, C) Example maximum intensity projection images of bulbar mitral/tufted cells (M/TCs; **A**) or external tufted cells (ETCs; **C**) visualized via SMI-32 staining, and the activity marker pS6. epl, external plexiform layer; mcl, mitral cell layer; gcl, granule cell layer; gl, glomerular layer. Arrows indicate pS6 positive M/TCs **(A)** or ETCs **(C)**; SMI-32 positive cells located in the epl (asterisks) were not analysed. Experimental design as in Fig. 2A. **(B, D)** Normalized pS6 intensity in M/TCs **(B)** or ETCs **(D)** from 6 sets of control and occluded mice. Empty circles represent individual cells and different colours indicate different mice; thick line shows mean ± SEM; ***, $p < 0.0001$.

Figure 4. Brief unilateral naris occlusion fails to induce structural plasticity at the axon initial segment or plasticity of intrinsic excitability in mitral/tufted cells. (A) Example average intensity projection image of bulbar mitral/tufted cells (M/TCs) visualized via SMI-32 staining and the AIS marker ankyrin-G (AnkG) in control and occluded mice. mcl, mitral cell layer; gcl, granule cell layer. The solid line indicates the emergence of the axonal process from the soma (asterisk); arrows indicate AIS start and end positions. **(B)** Mean ± SEM AIS start and end position for each group. **(C)** AIS distance from soma in M/TCs from control and occluded mice. **(D)** AIS length in M/TCs from control and occluded mice. In **(C,D)**, empty circles represent individual cells and different colours

indicate different mice; thick line shows mean ± SEM. **(E)** Diagram of whole-cell recordings from M/TCs. **(F)** Left: example current-clamp traces of single APs fired to threshold 10 ms somatic current injection by control and occluded M/TCs, and their associated phase plane plots. Right: Example current-clamp traces of multiple APs fired in response to a 130pA/500 ms somatic current injection in control and occluded cells. **(G)** Single action potential current threshold in control and occluded M/T cells. **(H)** Single action potential voltage threshold in control and occluded M/TCs. In **(G,H)**, empty circles represent individual cells; thick lines show mean ± SEM. **(I)** Input-output curve of 500 ms-duration current injection magnitude versus mean ± SEM spike number for each group.

Figure 5. Brief unilateral naris occlusion fails to induce structural plasticity at the axon initial segment or plasticity of intrinsic excitability in external tufted cells. (A) Example average intensity projection images of bulbar external tufted cells (ETCs) visualized via staining against cholecystokinin (CCK) and the AIS marker ankyrin-G (AnkG) in control and occluded mice. gl = glomerular layer; epl = external plexiform layer. **(B-I)** All conventions as in Fig. 4.

Figure 6. Brief unilateral naris occlusion decreases the expression of tyrosine hydroxylase in both DA subtypes (A) Example maximum intensity projection image of dopaminergic (DA) neurons visualized via tyrosine hydroxylase (TH) immunolabel in control and occluded mice. The TH images here are unaltered, and acquired with identical settings. gl, glomerular layer; epl, external plexiform layer. Arrows indicate TH positive DA cells representative of the two subtypes when defined by soma area. **(B)** Average glomerular layer density of TH-positive cells (of any soma size) in control and occluded mice. Empty circles represent individual image stacks and different colours indicate different mice; thick lines show mean ± SEM. **(C)** Mean normalised TH intensity in DA cells of any soma size, in three sets of control and occluded OBs. **(D)** Normalized TH intensity of DA cells with

soma size < 70 μm^2 (putative anaxonic cells), from 3 sets of control and occluded mice. **(E)** Normalized TH intensity of DA cells with soma size > 99 μm^2 (putative axon-bearing DA cells), from 3 sets of control and occluded mice. In **(D,E)**, empty circles represent individual cells and different colours indicate different mice; thick lines show mean ± SEM; ***, $p < 0.0001$. **(F)** Example average intensity projection images of TH label in DA cells with an identified ankyrin-G (AnkG)-positive AIS (arrows). The solid line indicates the emergence of the axonal process from the soma (asterisk). **(G)** Normalized TH intensity in AnkG-positive DA cells in control and occluded mice. Conventions as in **(D)**.

Figure 7. Brief unilateral naris occlusion does not alter the intrinsic excitability of monophasic/putative anaxonic DA cells (A) Diagram of whole-cell recordings from small fluorescent cells in DAT-tdTomato mice. **(B-E)** All conventions as in Fig. 4F-I.

Figure 8. Brief unilateral naris occlusion results in shorter axon initial segments and decreased intrinsic excitability in biphasic/putative axon-bearing DA cells. (A) Example average intensity projection images of bulbar axon-bearing DA cells, visualized via staining for tyrosine hydroxylase (TH) and the AIS marker ankyrin-G (AnkG) in control and occluded mice. DA AISs can be found either on a process originating directly from the soma (soma-origin), or on a process separated from the soma by one or more nodes (dendrite-origin). gl, glomerular layer; epl, external plexiform layer. The solid line indicates the emergence of the axonal process from the soma (asterisk); arrows indicate AIS start and end positions. **(B)** Left: schematic representation of soma-origin and dendrite-origin AISs. Right: mean ± SEM AIS start and end positions for each group. **(C)** AIS distance from soma in DA cells from control and occluded mice. For clarity, one outlier for distance from soma (62 µm, occluded group) is not included in the figure, but is included in all averages and analysis. **(D)** AIS length in

control and occluded mice. In **(C,D)**, empty symbols represent individual cells and different colours indicate different mice; circles indicate soma-origin AISs, triangles indicate dendrite-origin AISs; thick lines show mean ± SEM. **(E)** Diagram of whole-cell recordings from large fluorescent cells in DAT-tdTomato mice. **(F-I)** All conventions as in Fig. 4F-I. *, $p < 0.05$, **, $p < 0.01$, ***, $p < 0.001$.

TABLES

Target	Host	Supplier	Dilution
tyrosine hydroxylase (TH)	rabbit	Millipore	1:500
tyrosine hydroxylase (TH)	mouse	Millipore	1:500
tyrosine hydroxylase (TH)	chicken	Abcam	1:250
ankyrin-G (AnkG)	mouse 2a	NeuroMab	1:500
ankyrin-G (AnkG)	mouse 2b	NeuroMab	1:500
ankyrin-G (AnkG)	mouse 1	NeuroMab	1:500
Cholecystokinin (CCK)	rabbit	Immunostar	1:200
Neurofilament H Non-Phosphorylated (SMI-32)	mouse	Biolegend	1:1000
cFos	mouse	SantaCruz biotechnology	1:500
Phospho-S6 Ribosomal Protein (pS6)	rabbit	Cell Signaling	1:400
Olfactory Marker Protein (OMP)	goat	Wako	1:1000
Cleaved Caspase-3 (Casp3)	rabbit	Cell Signalling Technology	1:1000

Table 1. **Primary antibodies used**.

Mitral/tufted cells			
	Control (mean ± SEM, [n])	**Occluded** (mean ± SEM, [n])	**Test type, *p*-value**
PASSIVE PROPERTIES			
Membrane capacitance (pF)	66 ± 4, [24]	65 ± 4, [26]	t, 0.77
Resting membrane potential (mV)	-49.12 ± 1.318, [4]	-51.33 ± 1.535, [8]	t, 0.41
Input Resistance (MΩ)	135 ± 19, [24]	108 ± 11, [26]	MW, 0.33
ACTION POTENTIAL PROPERTIES			
Threshold (pA)	323 ± 45, [16]	317 ± 36, [23]	t, 0.92
Threshold (mV)	-39.86 ± 0.67, [16]	-37.80 ± 0.83, [23]	MW, 0.07
Max voltage reached (mV)	29.29 ± 1.64, [16]	30.81 ± 1.21, [23]	t, 0.45
Peak amplitude (mV)	69.15 ± 1.38, [16]	68.61 ± 1.28, [23]	t, 0.78
Width at half-height (ms)	0.41 ± 0.02, [15]	0.45 ± 0.02, [23]	t, 0.15
Rate of rise (max *dV/dt*, mV*ms)	366 ± 16, [16]	346 ± 12, [23]	t, 0.32
Onset rapidness (1/ms)	32.68 ± 1.28, [16]	27.34 ± 2.05, [23]	t, 0.054
Afterhyperpolarization (AHP, mV)	-54.12 ± 0.85, [22]	-53.88 ± 0.59, [24]	t, 0.82
AHP relative to threshold (mV)	16.24 ± 0.74, [22]	18.16 ± 0.80, [24]	t, 0.09
REPETITIVE FIRING PROPERTIES			
Rheobase (pA)	108 ± 17.72, [22]	122.2 ± 16.06, [25]	t, 0.55
Max number of action potentials	64.39 ± 6.33, [22]	58.75 ± 6.16, [25]	t, 0.53
First action potential delay (ms)	392 ± 16, [22]	368 ± 18, [25]	t, 0.33
Inter-spike interval CV	0.48 ± 0.07, [22]	0.38 ± 0.05, [26]	MW, 0.44

Table 2. Intrinsic electrophysiological properties of mitral/tufted cells (M/TCs).

Mean values ± SEM of passive, action potential and repetitive firing properties for control and occluded M/T cells. Statistical differences between groups were calculated with an unpaired t-test for normally-distributed data ("t") or with a Mann–Whitney test for non-normally distributed data ("MW").

External tufted cells			
	Control (mean ± SEM, [n])	**Occluded** (mean ± SEM, [n])	**Test type, *p*-value**
PASSIVE PROPERTIES			
Membrane capacitance (pF)	43.43 ± 2.13, [35]	41.92 ± 1.67, [57]	t, 0.58
Resting membrane potential (mV)	-57.33 ± 0.92, [36]	-56.58 ± 0.94, [64]	t, 0.60
Input Resistance (MΩ)	271 ± 27, [35]	242 ± 17, [57]	MW, 0.29
ACTION POTENTIAL PROPERTIES			
Threshold (pA)	103 ± 8, [35]	112 ± 7, [57]	MW, 0.50
Threshold (mV)	-39.10 ± 0.48, [35]	-38.56 ± 0.48, [57]	MW, 0.57
Max voltage reached (mV)	22.08 ± 1.18, [35]	22.69 ± 0.69, [57]	t, 0.64
Peak amplitude (mV)	61.17 ± 1.14, [35]	61.26 ± 0.82, [57]	t, 0.94
Width at half-height (ms)	0.53 ± 0.02, [35]	0.52 ± 0.01, [57]	MW, 0.94
Rate of rise (max *dV/dt*, mV*ms)	205 ± 7, [35]	211 ± 4, [57]	t, 0.44
Onset rapidness (1/ms)	29.65 ± 0.85, [30]	30.18 ± 0.94, [37]	MW, 0.42
Afterhyperpolarization (AHP, mV)	-52.04 ± 0.45, [23]	-52.30 ± 0.60, [38]	t, 0.76
AHP relative to threshold (mV)	15.41 ± 0.85, [23]	17.14 ± 0.58, [38]	t, 0.09
REPETITIVE FIRING PROPERTIES			
Rheobase (pA)	41 ± 8 pA, [23]	45 ± 7 pA, [38]	MW, 0.73
Max number of action potentials	61 ± 4, [30]	56 ± 3, [45]	t, 0.34
First action potential delay (ms)	187 ± 23, [23]	171 ± 22, [38]	t, 0.63
Inter-spike interval CV	0.33 ± 0.04, [30]	0.38 ± 0.04, [45]	MW, 0.65

Table 3. Intrinsic electrophysiological properties of external tufted cells (ETCs).

Mean values ± SEM of passive, action potential and repetitive firing properties for control and occluded ET cells. Statistical differences between groups were calculated with an unpaired t-test for normally-distributed data ("t") or with a Mann–Whitney test for non-normally distributed data ("MW").

Monophasic dopaminergic cells (putative anaxonic)			
	Control (mean ± SEM, [n])	**Occluded** (mean ± SEM, [n])	**Test type, *p*-value**
PASSIVE PROPERTIES			
Membrane capacitance (pF)	19.17 ± 2.18, [15]	20.81 ± 1.77, [12]	MW, 0.37
Resting membrane potential (mV)	-77.87 ± 1.92, [15]	-70.50 ± 2.49, [12]	t, 0.03
Input Resistance (MΩ)	960 ± 272, [15]	694 ± 223, [12]	MW, 0.21
ACTION POTENTIAL PROPERTIES			
Threshold (pA)	129.7 ± 19.2, [13]	160 ± 29.23, [11]	t, 0.38
Threshold (mV)	-30.47 ± 1.09, [13]	-30.70 ± 1.37, [11]	MW, 0.86
Max voltage reached (mV)	19.55 ± 2.42, [13]	23.19 ± 1.78, [11]	t, 0.26
Peak amplitude (mV)	50.01 ± 2.35, [13]	53.89 ± 2.89, [11]	MW, 0.22
Width at half-height (ms)	0.54 ± 0.03, [13]	0.55 ± 0.03, [11]	t, 0.80
Rate of rise (max *dV/dt*, mV*ms)	240.7 ± 15.82, [13]	254.8 ± 19.63, [11]	t, 0.58
Onset rapidness (1/ms)	3.94 ± 0.29, [13]	3.23 ± 0.20, [11]	t, 0.06
Afterhyperpolarization (AHP, mV)	-54.39 ± 1.44, [14]	-54.83 ± 1.34, [12]	t, 0.83
AHP relative to threshold (mV)	24.58 ± 1.27, [14]	25.87 ± 1.49, [12]	t, 0.51
REPETITIVE FIRING PROPERTIES			
Rheobase (pA)	61 ± 19, [14]	86 ± 20, [12]	t, 0.23
Max number of action potentials	10 ± 2, [14]	7 ± 2, [12]	MW, 0.16
First action potential delay (ms)	169.2 ± 38.99, [14]	91.34 ± 21.92, [12]	t(W), 0.10
Inter-spike interval CV	0.28 ± 0.04, [14]	0.26 ± 0.04, [11]	t, 0.72

Table 4. Intrinsic electrophysiological properties of monophasic/putative anaxonic DA cells.

Mean values ± SEM of passive, action potential and repetitive firing properties for control and occluded monophasic/putative anaxonic DA cells. Statistical differences between groups were calculated with an unpaired t-test for normally-distributed data ("t"; with Welch's correction "t(W)") or with a Mann–Whitney test for non-normally distributed data ("MW"). Grey shading indicates statistically

Biphasic dopaminergic cells (putative axon-bearing)			
	Control (mean ± SEM, [n])	**Occluded** (mean ± SEM, [n])	**Test type, *p*-value**
PASSIVE PROPERTIES			
Membrane capacitance (pF)	22.07 ± 2.21, [11]	21.72 ± 2.07, [10]	t, 0.91
Resting membrane potential (mV)	-74.27 ± 2.94, [11]	-77.50 ± 1.73, [10]	MW, 0.65
Input Resistance (MΩ)	573 ± 115, [11]	631 ± 117, [10]	MW, 0.46
ACTION POTENTIAL PROPERTIES			
Threshold (pA)	102 ± 11, [9]	148 ± 16, [10]	t, 0.035
Threshold (mV)	-32.58 ± 0.99, [9]	-28.57 ± 0.78, [10]	t, 0.005
Max voltage reached (mV)	17.61 ± 3.96, [9]	19.87 ± 3.61, [10]	t, 0.68
Peak amplitude (mV)	50.17 ± 4.63, [9]	48.43 ± 3.60, [10]	t, 0.76
Width at half-height (ms)	0.50 ± 0.04, [9]	0.53 ± 0.03, [10]	t, 0.55
Rate of rise (max *dV/dt*, mV*ms)	250 ± 31, [9]	227 ± 17, [10]	t, 0.51
Onset rapidness (1/ms)	8.22 ± 1.66, [9]	6.63 ± 1.39, [10]	MW, 0.72
Afterhyperpolarization (AHP, mV)	-55.13 ± 1.50, [11]	-54.27 ± 2.71, [10]	MW, 0.55
AHP relative to threshold (mV)	24.46 ± 1.30, [11]	25.17 ± 2.64, [10]	MW, 0.32
REPETITIVE FIRING PROPERTIES			
Rheobase (pA)	32 ± 13, [11]	25 ± 5, [10]	MW, 0.73
Max number of action potentials	21 ± 4, [11]	15 ± 3, [10]	t, 0.23
First action potential delay (ms)	273 ± 45, [11]	188 ± 50, [10]	t, 0.22
Inter-spike interval CV	0.24 ± 0.03, [10]	0.22 ± 0.06, [9]	MW, 0.45

Table 5. Intrinsic electrophysiological properties of biphasic/putative axon-bearing DA cells.

Mean values ± SEM of passive, action potential and repetitive firing properties for control and occluded biphasic/putative axon-bearing DA cells. Statistical differences between groups were calculated with an unpaired t-test for normally-distributed data ("t") or with a Mann–Whitney test for non-normally distributed data ("MW"). Grey shading indicates statistically significant difference.

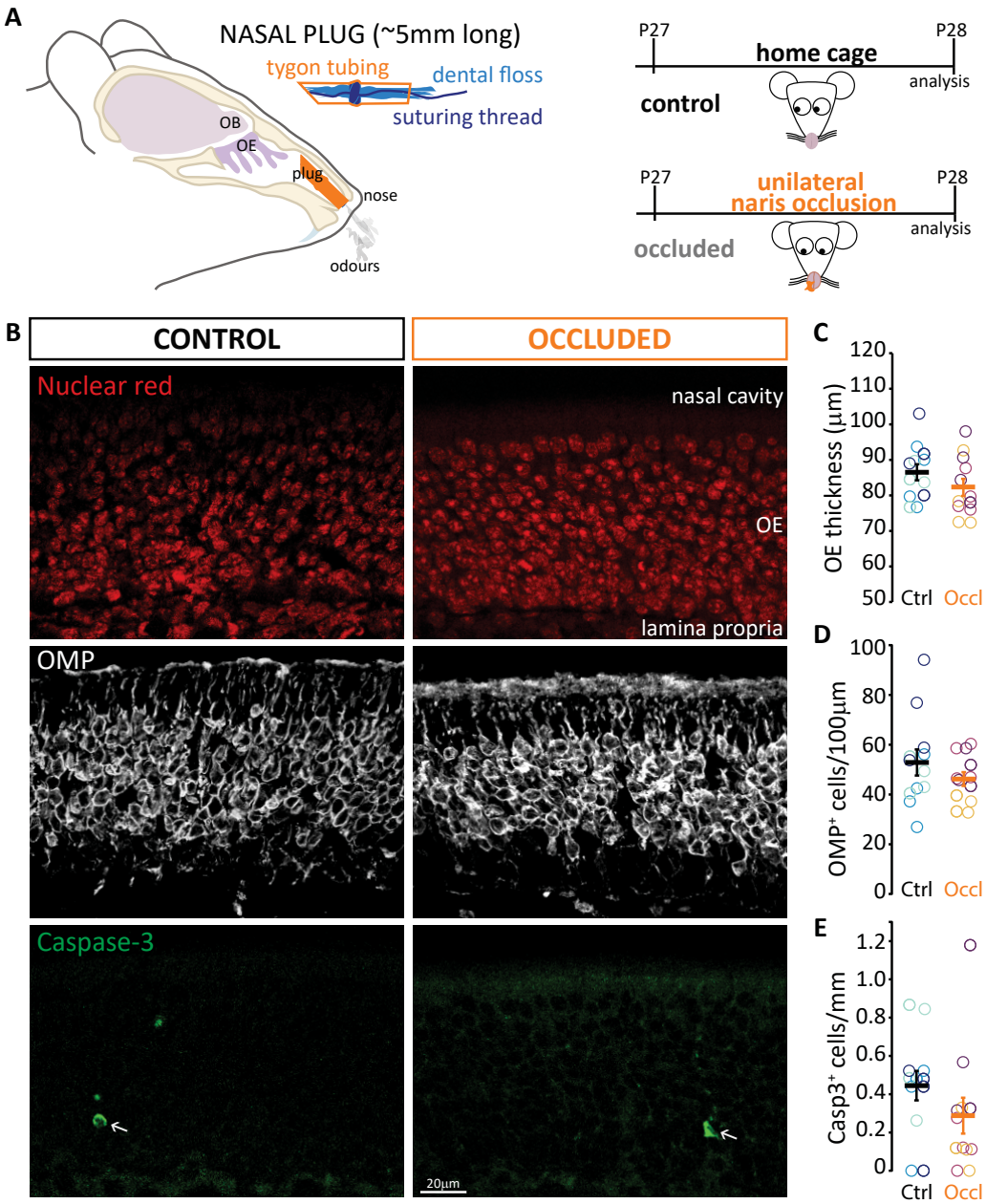
A
NASAL PLUG (~5mm long)
tygon tubing
dental floss
suturing thread
OB
OE
plug
nose
odours
P27
home cage
P28
analysis
control
P27
unilateral
naris occlusion
P28
analysis
occluded
B
CONTROL
OCCLUDED
Nuclear red
nasal cavity
OE
lamina propria
OMP
Caspase-3
20µm
C
OE thickness (µm)
120
110
100
90
80
70
60
50
Ctrl
Occl
D
OMP⁺ cells/100µm
100
80
60
40
20
0
Ctrl
Occl
E
Casp3⁺ cells/mm
1.2
1.0
0.8
0.6
0.4
0.2
0
Ctrl
Occl

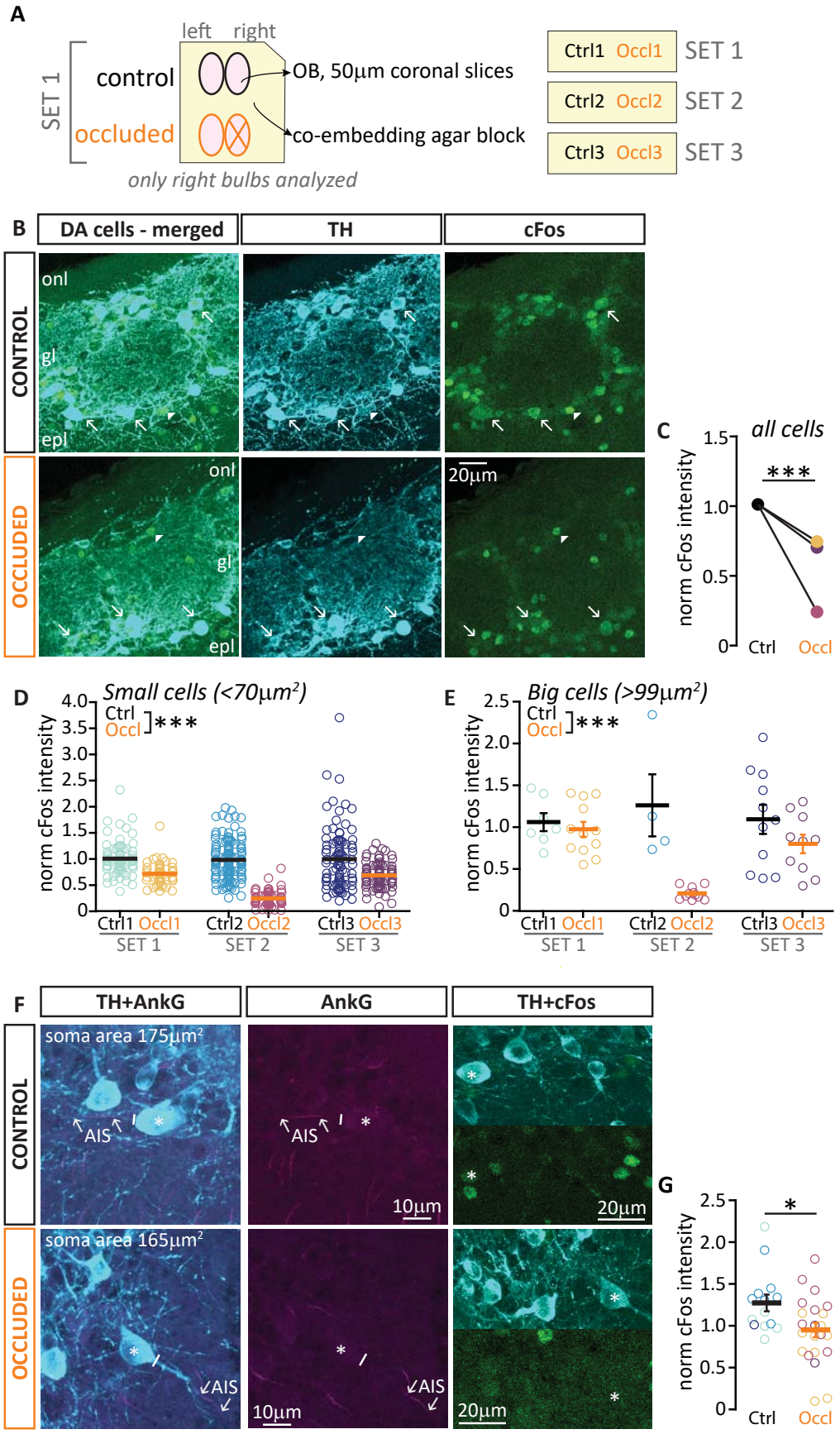
A
left right
SET 1
control
occluded
OB, 50µm coronal slices
co-embedding agar block
only right bulbs analyzed
Ctrl1 Occl1 SET 1
Ctrl2 Occl2 SET 2
Ctrl3 Occl3 SET 3
B
DA cells - merged
TH
cFos
CONTROL
OCCLUDED
onl
gl
epl
20µm
C
all cells
***
norm cFos intensity
Ctrl
Occl
D
Small cells (<70µm²)
Ctrl
Occl
***
norm cFos intensity
Ctrl1 Occl1
Ctrl2 Occl2
Ctrl3 Occl3
SET 1
SET 2
SET 3
E
Big cells (>99µm²)
Ctrl
Occl
***
norm cFos intensity
Ctrl1 Occl1
Ctrl2 Occl2
Ctrl3 Occl3
SET 1
SET 2
SET 3
F
TH+AnkG
AnkG
TH+cFos
CONTROL
OCCLUDED
soma area 175µm²
soma area 165µm²
AIS
10µm
20µm
G
*
norm cFos intensity
Ctrl
Occl

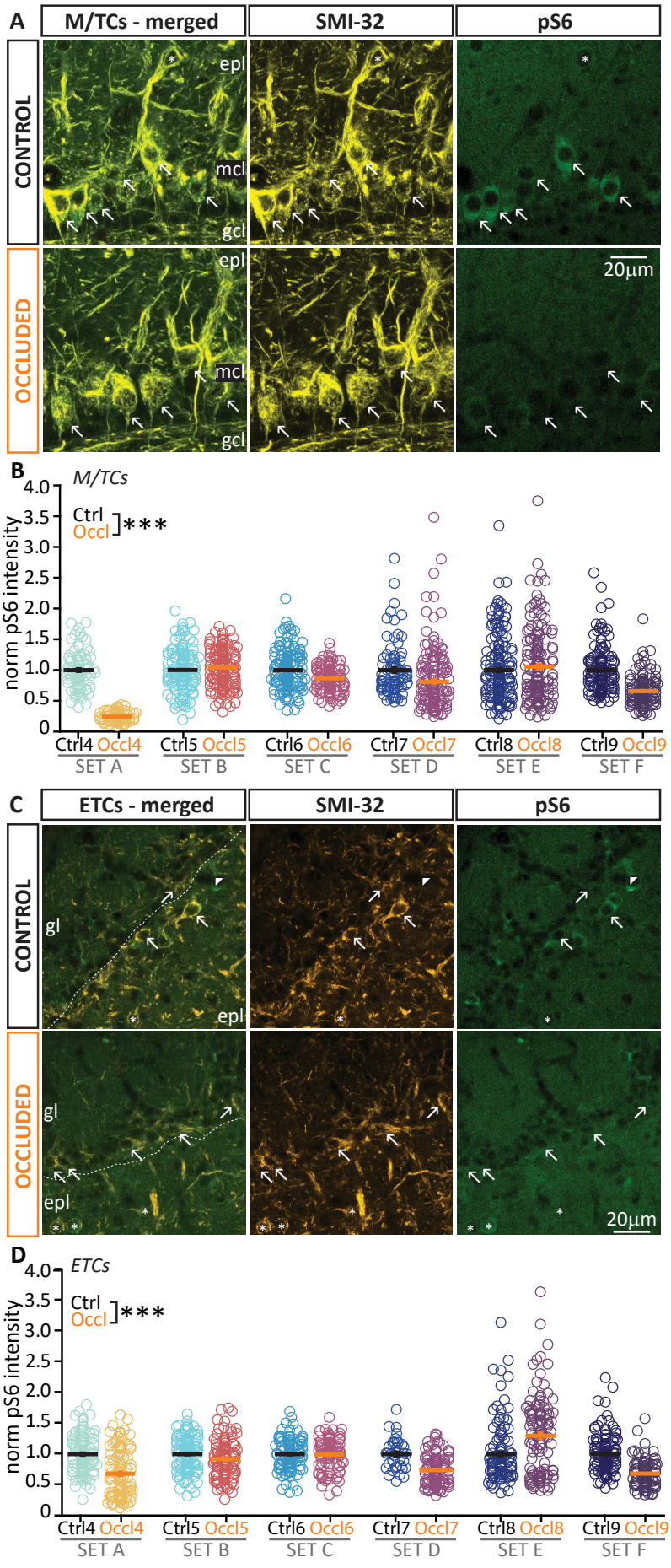
A
M/TCs - merged
SMI-32
pS6
CONTROL
OCCLUDED
epl
mcl
gcl
20µm
B
M/TCs
norm pS6 intensity
Ctrl
Occl
***
Ctrl4 Occl4
SET A
Ctrl5 Occl5
SET B
Ctrl6 Occl6
SET C
Ctrl7 Occl7
SET D
Ctrl8 Occl8
SET E
Ctrl9 Occl9
SET F
C
ETCs - merged
SMI-32
pS6
CONTROL
OCCLUDED
gl
epl
20µm
D
ETCs
norm pS6 intensity
Ctrl
Occl
***
Ctrl4 Occl4
SET A
Ctrl5 Occl5
SET B
Ctrl6 Occl6
SET C
Ctrl7 Occl7
SET D
Ctrl8 Occl8
SET E
Ctrl9 Occl9
SET F

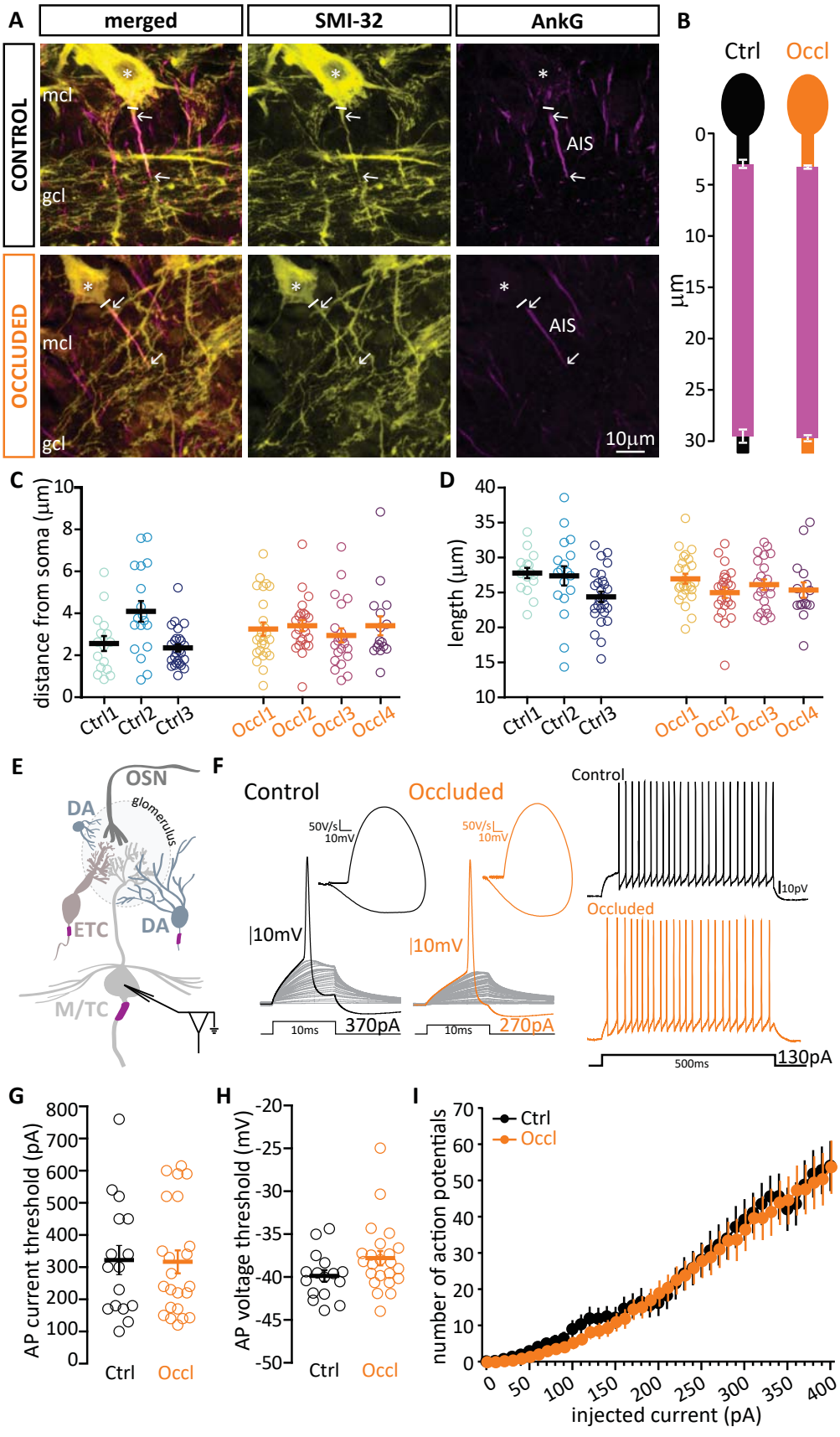
A
merged
SMI-32
AnkG
CONTROL
OCCLUDED
mcl
gcl
AIS
10µm
B
Ctrl
Occl
µm
C
distance from soma (µm)
Ctrl1
Ctrl2
Ctrl3
Occl1
Occl2
Occl3
Occl4
D
length (µm)
E
OSN
DA
glomerulus
ETC
M/TC
F
Control
Occluded
50V/s
10mV
370pA
270pA
10ms
500ms
130pA
G
AP current threshold (pA)
H
AP voltage threshold (mV)
I
number of action potentials
injected current (pA)

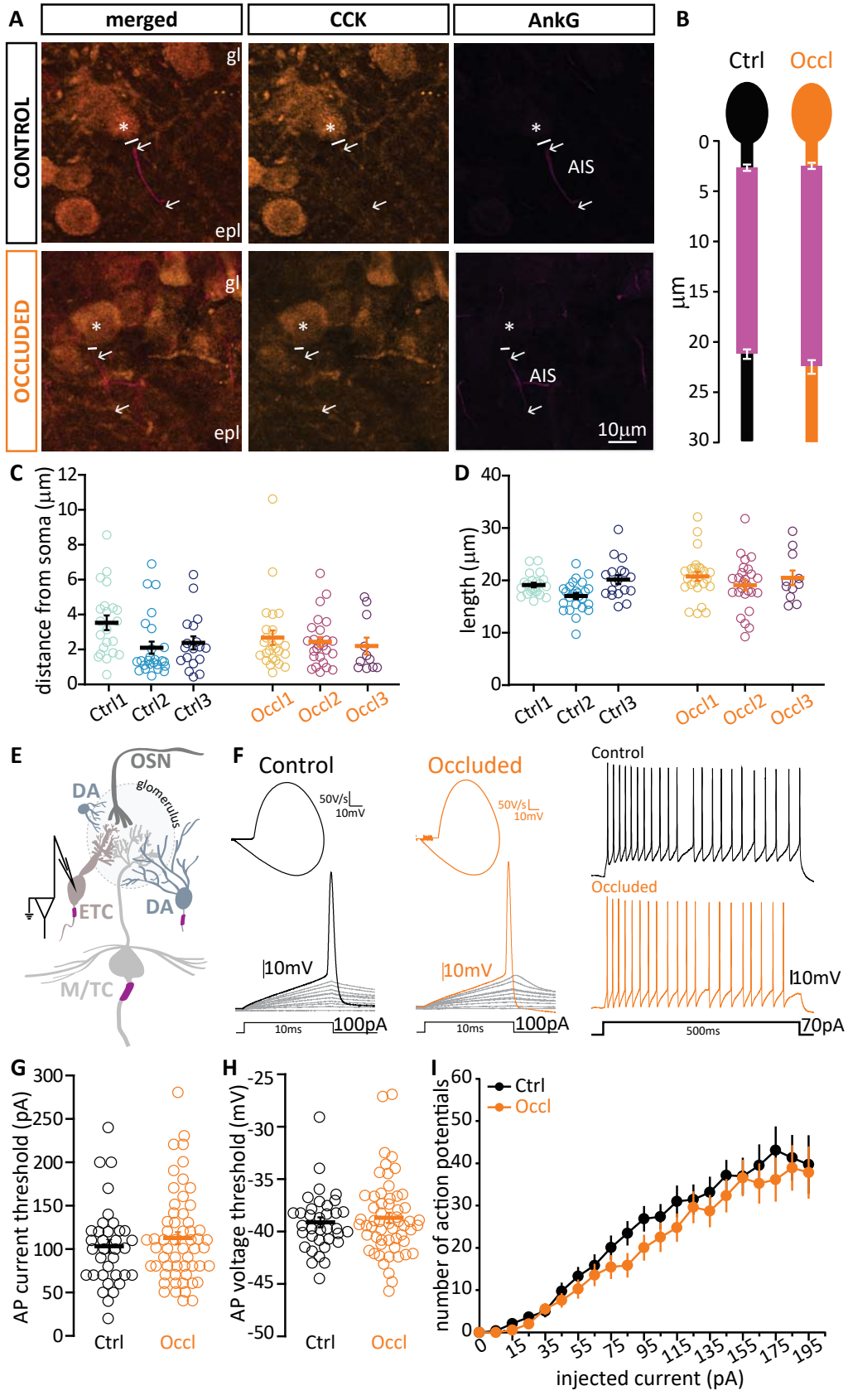
A
merged
CCK
AnkG
CONTROL
OCCLUDED
gl
epl
AIS
10µm
B
Ctrl
Occl
µm
C
distance from soma (µm)
Ctrl1
Ctrl2
Ctrl3
Occl1
Occl2
Occl3
D
length (µm)
E
OSN
DA
glomerulus
ETC
M/TC
F
Control
Occluded
50V/s
10mV
100pA
10ms
500ms
70pA
G
AP current threshold (pA)
H
AP voltage threshold (mV)
I
number of action potentials
injected current (pA)

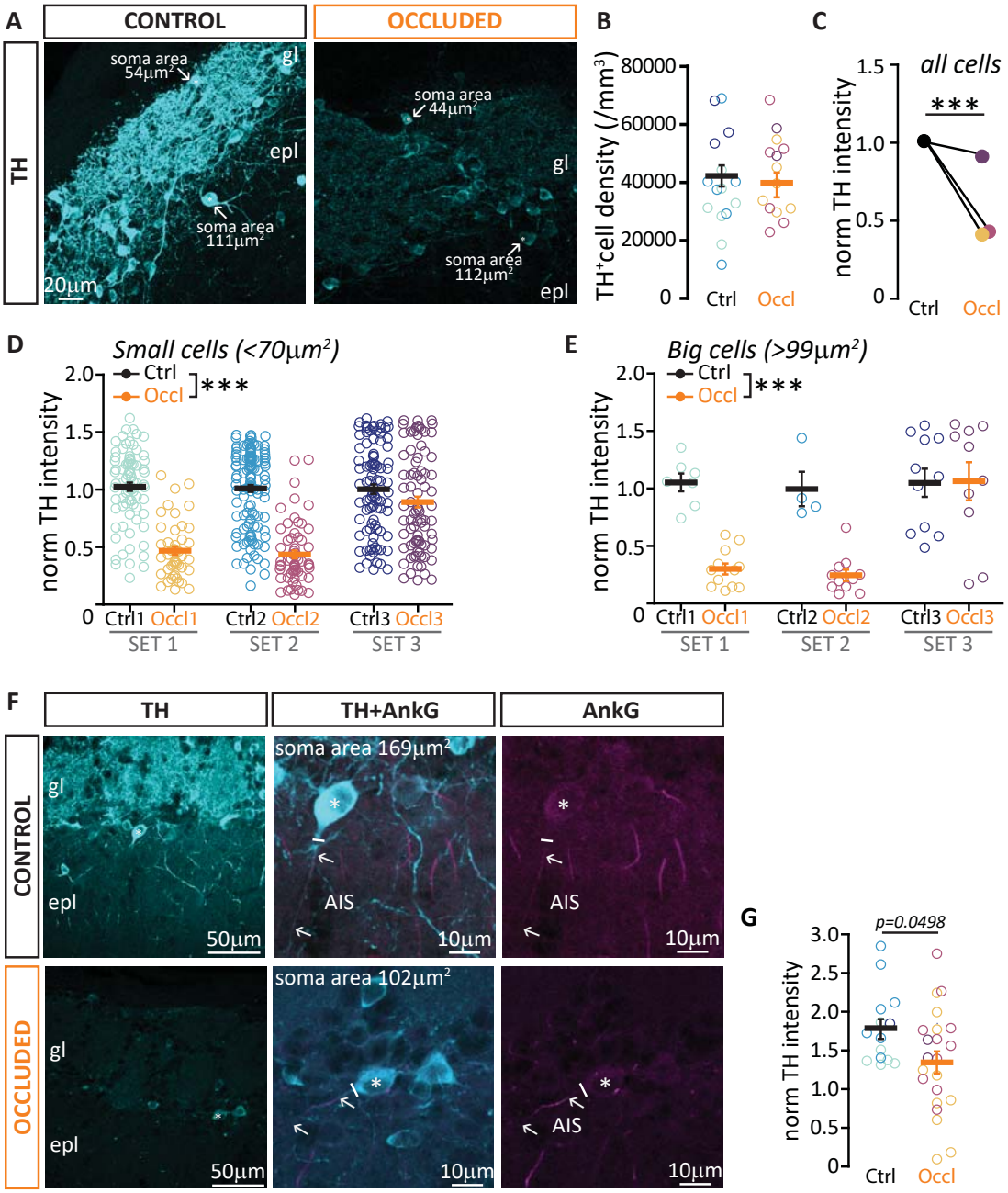
A
CONTROL
OCCLUDED
TH
soma area 54µm²
gl
epl
soma area 111µm²
20µm
soma area 44µm²
gl
soma area 112µm²
epl
B
TH⁺cell density (/mm³)
80000
60000
40000
20000
0
Ctrl
Occl
C
all cells
***
norm TH intensity
1.5
1.0
0.5
0
Ctrl
Occl
D
Small cells (<70µm²)
Ctrl
Occl
***
norm TH intensity
2.0
1.5
1.0
0.5
0
Ctrl1 Occl1
Ctrl2 Occl2
Ctrl3 Occl3
SET 1
SET 2
SET 3
E
Big cells (>99µm²)
Ctrl
Occl
***
norm TH intensity
2.0
1.5
1.0
0.5
0
Ctrl1 Occl1
Ctrl2 Occl2
Ctrl3 Occl3
SET 1
SET 2
SET 3
F
TH
TH+AnkG
AnkG
CONTROL
OCCLUDED
gl
epl
50µm
soma area 169µm²
AIS
10µm
soma area 102µm²
G
p=0.0498
norm TH intensity
3.0
2.5
2.0
1.5
1.0
0.5
0
Ctrl
Occl

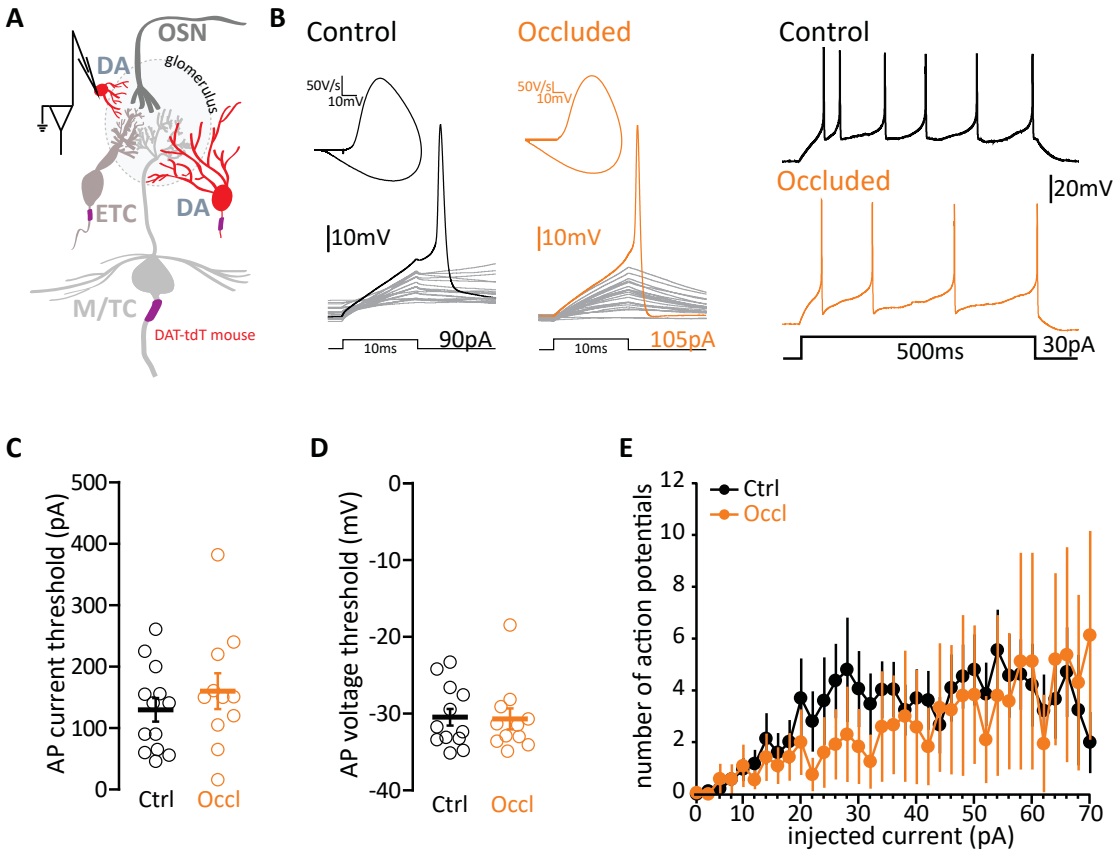
A
OSN
DA
glomerulus
ETC
DA
M/TC
DAT-tdT mouse
B
Control
50V/s
10mV
10mV
10ms
90pA
Occluded
50V/s
10mV
10mV
10ms
105pA
Control
Occluded
20mV
500ms
30pA
C
AP current threshold (pA)
500
400
300
200
100
0
Ctrl
Occl
D
AP voltage threshold (mV)
0
-10
-20
-30
-40
Ctrl
Occl
E
number of action potentials
12
10
8
6
4
2
0
Ctrl
Occl
0
10
20
30
40
50
60
70
injected current (pA)

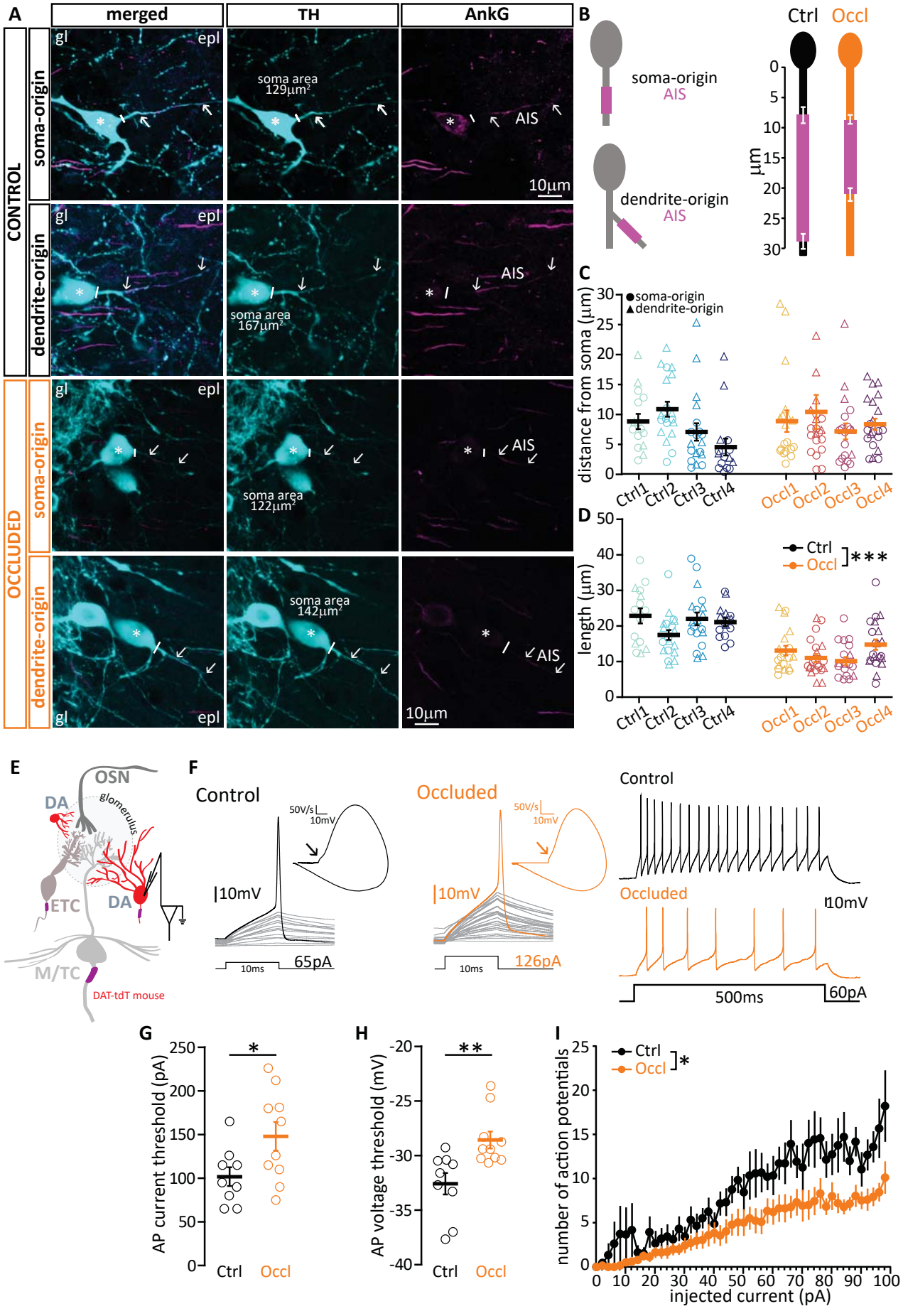
A
merged
TH
AnkG
CONTROL
OCCLUDED
soma-origin
dendrite-origin
gl
epl
soma area 129µm²
soma area 167µm²
soma area 122µm²
soma area 142µm²
AIS
10µm
B
soma-origin
AIS
dendrite-origin
AIS
Ctrl
Occl
µm
C
soma-origin
dendrite-origin
distance from soma (µm)
Ctrl1
Ctrl2
Ctrl3
Ctrl4
Occl1
Occl2
Occl3
Occl4
D
length (µm)
Ctrl
Occl
***
E
OSN
DA
glomerulus
ETC
DA
M/TC
DAT-tdT mouse
F
Control
50V/s
10mV
10mV
10ms
65pA
Occluded
126pA
Control
Occluded
500ms
60pA
G
AP current threshold (pA)
*
Ctrl
Occl
H
AP voltage threshold (mV)
**
I
number of action potentials
injected current (pA)
*